Corrosion performance comparison of CoCrFeNi-based high-entropy alloys and austenitic stainless steels in acidic oxidizing chloride solutions

V.A. Vorkel,[1]* R.I. Bogdanov,[2] N.A. Pukhareva,[2] V.E. Ignatenko,[1] A.A. Rybkina,[1] A.V. Voennov[3] and A.I. Marshakov[1]

[1]A.N. Frumkin Institute of Physical Chemistry and Electrochemistry, Russian Academy of Sciences, Leninsky pr. 31, 119071 Moscow, Russian Federation
[2]Department of Materials Science, National Research Nuclear University MEPhI, 115409, Moscow, Russian Federation
[3]Federal State Unitary Enterprise "NL Dukhov All-Russian Scientific Research Institute of Automation" (VNIIA), 127055, Moscow, Russian Federation
**E-mail: vvorkel@gmail.ru*

Abstract

The long-term corrosion resistance of the CoCrFeNi-based high-entropy alloys and austenitic stainless steels were investigated. According to the gravimetric tests, in the 0.6 M NaCl + 0.1 M HCl solution with and without 10 mM H_2O_2 the general corrosion rates of Mo-containing $CoCrFeNiMo_{0.4}$ and AISI 316L were higher than that of AISI 304 due to the uneven distribution of Cr and Mo and the lower Cr content, respectively. However, both steels were considerably prone to intergranular corrosion in the presence of hydrogen peroxide. As for $CoCrFeNiMo_{0.4}$, only the matrix areas depleted in Mo and located proximately to the (Cr, Mo)-rich σ-phase were slightly susceptible to pitting corrosion. The corrosion rate of $CoCrFeNiMo_{0.4}$ was also significantly lower than those of both steels in the 0.4 M $FeCl_3$ solution. The small σ-phase content in the $CoCrFeNiMo_{0.4}$ microstructure and overall Cr and Mo distribution effectively suppressed its selective corrosion. According to the anodic curves of $CoCrFeNiMo_{0.4}$, the onset of metastable pitting was possible, which could also explain the alloy's weight loss during the long-term corrosion tests. $CoCrFeNiAl_{0.5}Cu_{0.5}$ did not passivate in any test solution, and the oxidizers intensified its active dissolution initiated in the Cu-based precipitates. Comparing the results of gravimetric tests and polarization measurements demonstrated quantitative discrepancies between them due to the onset of a steady state during the long-term tests and with the determination of the average corrosion rate rather than the instantaneous one. This phenomenon should be carefully considered when justifying the alloys' potential applications.

Received: June 11, 2024. Published: July 4, 2024 doi: 10.17675/2305-6894-2024-13-3-3

Keywords: *high-entropy alloy, selective dissolution, gravimetric test, corrosion rate, oxidizer.*

1. Introduction

Currently, high-entropy alloys (HEAs) based on 3d-transition metals, mainly Co-Cr-Fe-Ni systems, are being widely studied. Alloying with additional elements such as Mo, Al, and Cu allows the properties of the material to be varied, improving its mechanical and/or corrosion characteristics [1, 2].

The effect of molybdenum on the corrosion resistance of the Co-Cr-Fe-Ni HEAs was studied in Refs. [3–9]. Hu *et al*. [3] performed a study of the $CoCrFeNiMo_x$ ($x = 0-1$) corrosion behavior in 0.005 M H_2SO_4 and showed that Mo, on the one hand, contributed to the passive layer enrichment with Cr_2O_3. On the other hand, an increase in the Mo concentration led to an increase in the relative content of the σ-phase, which was cathodic to the FCC matrix. When x equalled 0.6, the positive effect of Cr_2O_3-enrichment on the corrosion resistance surpassed the negative effect of the FCC matrix dissolution. Dai *et al*. [4] conducted immersion tests of the $CoCrFeNiMo_x$ ($x = 0$; 0.1; 0.3; 0.6) in 6 wt.% $FeCl_3$ + 0.05 M HCl at 60°C and showed that the HEAs with $x = 0$ and $x = 0.1$ were susceptible to pitting corrosion, and it was much more intense on the Mo-free alloy's surface. In the case of $CoCrFeNiMo_{0.3}$ the areas around the (Cr, Mo)-enriched phases were preferentially dissolved, and in the case of $CoCrFeNiMo_{0.6}$ the entire (Cr, Mo)-depleted matrix was prone to localized corrosion. Wang *et al*. [5, 6] subjected single-phase $Co_5Cr_{25}Fe_{25}Ni_{40}Mo_5$ (at.%) and $Co_5Cr_{15}Fe_{10}Ni_{60}Mo_{10}$ (at.%) to the passivation treatment in the 0.05 M H_2SO_4 background solution and obtained a bilayer protective film [6]. The inner barrier layer consisted mainly of Cr_2O_3, whereas the outer layer was enriched in the Cr(III) hydroxide, as well as in the Mo(IV) and Mo(VI) oxides [6]. The film provided high resistance to the localized corrosion during subsequent potentiodynamic anodic polarization in the background solution with the addition of NaCl up to 5 M [5]. Wang *et al*. [7] carried out potentiostatic polarization of the CoCrFeNiMo HEA in the CO_2-saturated 50 g/L NaCl solution (pH 3.8). It was shown that an increase in the potential of the passive film formation resulted in a decrease in the Cr and Mo content in the film. However, the local passive films, formed on the σ- and μ-phases, were enriched in Cr and Mo oxides than those formed on the FCC matrix. At potentials corresponding to the transpassive region, the local passive films, formed on the matrix, dissolved, and the σ- and μ-phases remained protected, which led to the selective corrosion. Corrosion studies of the HEAs based on the Co-Cr-Fe-Ni system with the additions of Mo, Al, Ti, Mn, Cu, V, Nb, La, Sn, Ge, Ga, Si were carried out in the 0.6 M NaCl and 0.5 M H_2SO_4 solutions. A thorough analysis of the obtained results is presented in Refs. [8, 9]. It was shown [9] that, among HEAs of various compositions, $CoCrFeNiMo_{0.4}$ is one of the most resistant to general corrosion in 0.5 M H_2SO_4, surpassing AISI 304 stainless steel (SS).

The effect of aluminium and copper on the corrosion resistance of the Co-Cr-Fe-Ni HEAs was studied in Refs. [10–15]. Fu *et al*. [10] showed that a slight increase in the Al concentration improved the corrosion resistance of $CoCrFeNiAl_x$ ($x = 0.1$, 0.3) in 0.5 M H_2SO_4 due to an increased content ratio of the chromium, iron and aluminium oxides to their

hydroxides in the passive layer, which ensured the formation of a denser protective film. However, increasing Al content was detrimental to general corrosion resistance in 0.5 M HCl. Uniform corrosion with the preferential dissolution of some crystallographic planes was observed. Wei and Qin [11] showed that, during the initial corrosion period of the eutectic dual-phase $CoCrFeNi_{2.1}Al$ HEA in 0.5 M H_2SO_4, the FCC and BCC phases formed a microgalvanic couple, in which the BCC phase, enriched in aluminium and nickel and depleted in chromium, acted as an anode. As the selective corrosion of the BCC phase proceeded, the entire lamellar structural constituent (FCC+BCC) began to preferentially dissolve compared to the irregular regions. Song *et al*. [12] subjected the eutectic $CoCrFeNi_{2.1}Al$ HEA to potentiostatic polarization in the 0.005 M H_2SO_4+0.05 M NaCl solution at various temperatures. Only pitting corrosion occurred at 5°C. At more elevated temperatures (25, 40, and 60°C), selective corrosion developed along with pitting. The preferential dissolution of the (Al, Ni)-rich BCC phase accelerated with increasing temperature and became the main type of damage. Li *et al*. [13] showed that the $CoCrFeNiAl_{0.5}Cu_{0.5}$ HEA with the FCC structure could passivate in 0.5 M H_2SO_4. However, there was no passive region on the polarization curves obtained in 0.5 NaCl. This HEA's corrosion resistance was inferior to that of single-phase $CoCrFeNiAlCu_{0.5}$ with the BCC structure but superior to that of dual-phase $CoCrFeNiAl_{1.5}Cu_{0.5}$ with the duplex structure (FCC and BCC). Li *et al*. [14] managed to enhance the corrosion resistance of the CoCrFeNiCu HEA in 0.6 M NaCl by the Cu segregation improvement and grain refinement, which resulted in the increased passive film stability. Chen *et al*. [15] significantly improved the corrosion resistance of the $CoCrFeNiAl_{0.3}Cu_{0.3}$ HEA by its passivation treatment in 30 wt.% HNO_3 and then in 1 wt.% NaOH. However, at a higher Cu content, the effectiveness of this procedure was insufficient to suppress the negative effect of the Cu-based phases' preferential dissolution.

Thus, most HEAs of the CoCrFeNiX (X = Mo; Al; Cu) system are prone to passivation in acidic solutions, and their corrosion resistance strongly depends on the alloy's microstructure, composition of the passive film, and its stability. The latter can be diminished due to the alloys' microstructural heterogeneity characterized by different phases and segregations. The positive effect of Mo on the HEAs' passivation was noted. At the same time, in the case of $CoCrFeNiMo_x$, with an increase of x up to 0.4, the strength and hardness increase without substantial ductility degradation [2]. As the Mo concentration becomes $x \geq 0.5$, the HEAs embrittle due to the high content of the σ-phase. Simultaneous alloying with Cu and Al up to $x \geq 0.5$ contributes to the production of a relatively strong and ductile alloy [16, 17] prone to passivation in an acidic medium.

In the studies of HEAs corrosion, researchers usually used dilute H_2SO_4 solutions, in which the main oxidizing agent was dissolved oxygen. According to the aforementioned studies [4, 5, 7, 10, 11–13], the passive state stability and the HEAs corrosion behavior change with the presence of chloride ions in the solution and, as was shown in our previous publication [18], with the addition of different types of strong oxidizers (H_2O_2, $FeCl_3$). Given

the above, acidic NaCl solutions with and without H_2O_2 as well as a $FeCl_3$ solution were used in the present work.

The duration of immersion tests in Ref. [4] did not exceed 120 hours, in Ref. [10] – 15 days, in Ref. [11] – 30 days. The specimens were exposed to the solutions in order to further investigate the surfaces, analyse the morphology of defects, and specify the type of corrosion damage. In Ref. [2], the authors determined the corrosion current density by obtaining the polarization curves and used its value in calculations to estimate the instantaneous rate of general corrosion. However, the most reliable approach to determining the long-term corrosion resistance is to establish the alloy's corrosion rates based on the gravimetric analysis. Such laboratory and especially field tests are essential to justify the possibility of the alloy's application and ensure safe and reliable operation by predicting the alloy's long-term behavior and the evolution of its properties.

The purpose of this work was to determine the long-term corrosion behavior and resistance of the CoCrFeNiX system (X = Mo; Al, Cu) HEAs in the acidic chloride solutions containing different types of the oxidizers. The obtained results were compared with the electrochemical properties of these HEAs. The properties of HEAs are often set against the properties of SSs, so the HEAs' corrosion behavior was also compared with the characteristics of commercial austenitic steels AISI 304 and AISI 316L, which are widely used in industry. These SSs are resistant to general corrosion but susceptible to local corrosion in solutions containing chloride ions and an oxidizing agent.

2. Materials and Methods

2.1. Materials and microstructural characterization

The $CoCrFeNiMo_{0.4}$, CoCrFeNiMo, and $CoCrFeNiAl_{0.5}Cu_{0.5}$ HEAs, as well as commercial austenitic SSs AISI 304 and AISI 316L, were investigated. The results of microstructure characterization and gravimetric rests of the CoCrFeNiMo HEA are presented in Ref. [18]. The nominal compositions of the HEAs and SSs [19] are given in Table 1 and Table 2, respectively.

Commercially pure metals (with purity higher than 99%) were used. The HEAs preparation was carried out *via* the arc melting method under the protection of a Zr-gettered Ar-flowing atmosphere in an arc furnace MIFI-9. First, the pressure in the working chamber was reduced from atmospheric to the value of $7 \cdot 10^4$ Pa. Then the continuous purging with Ar was maintained during the entire process of the alloys' preparation. The ingots were flipped and remelted 7 times to minimize chemical inhomogeneity and then directly solidified in a water-cooled copper mold. The alloys were subsequently annealed at 900°C for 1 h in a vacuum furnace SSHVE-1.2,5 and then with the furnace cooled to relieve residual stresses. The ingots were cut into specimens. The specimens were then grinded and polished by circles with the abrasiveness of P80 to P2500 and diamond suspensions with particle dispersion of 9 to 0.01 μm, then cleaned in an ultrasonic bath, degreased with ethanol, and washed with distilled water.

Table 1. Compositions of the HEAs.

Alloy	Ratio type	Element content						
		Co	**Cr**	**Fe**	**Ni**	**Mo**	**Al**	**Cu**
$CoCrFeNiMo_{0.4}$	at.%	22.7	22.7	22.7	22.7	9.1	–	–
	wt.%	22.3	19.7	21.2	22.3	14.5	–	–
CoCrFeNiMo	at.%	20.0	20.0	20.0	20.0	20.0	–	–
	wt.%	18.3	16.2	17.4	18.3	29.9	–	–
$CoCrFeNiAl_{0.5}Cu_{0.5}$	at.%	20.0	20.0	20.0	20.0	–	10.0	10.0
	wt.%	21.8	19.2	20.6	21.7	–	5.0	11.7

Table 2. Compositions of the SSs.

Steel	Element content (wt.%)					
	Fe	**C**	**Cr**	**Ni**	**Mn**	**Mo**
AISI 304	Bal.	0.08	19.0	9.5	2.0	–
AISI 316L	Bal.	0.03	17.0	12.0	2.0	2.5

The microstructure of the specimens and the morphology of their surfaces were studied using a scanning electron microscope (SEM) Carl Zeiss EVO 50. The accelerating voltage was 20 kV, and the beam current was 750 pA. The elemental composition and distribution of elements were analysed using an energy-dispersive spectrometer (EDS) INCA 350x-Act, equipped with a silicon drift detector, at 10 kV. X-Ray diffraction (XRD) measurements were performed on a Bruker D8 Advance diffractometer to investigate the HEAs' phase composition. The characteristic K_α radiation of a copper anode with a wavelength of 1.54060 Å was used. The measurements were carried out in the symmetric Bragg–Brentano geometry (θ–2θ). The spectra were decoded using the DIFFRAC.EVA software and international database ICDD PDF-2.

2.2. Corrosion tests

Dimensions of the specimens were 50 mm×10 mm×5 mm for the gravimetric tests. The tests were carried out using different acidic chloride solutions (Table 3). The solutions were prepared from reagent-grade chemicals, supplied by Labtech Ltd, and distilled water. For convenience, the test solutions were designated as S1, S2 (with the oxygen-containing oxidizer H_2O_2), and S3 (the cationic oxidizer $FeCl_3$) in accordance with Table 3. During the corrosion tests and electrochemical measurements, the solutions were naturally aerated at 22±1°C. It was shown in Ref. [18] that the weight losses of the CoCrFeNiMo HEA and SS 430 are low and can be reliably detected only after more than 3000 h of testing.

Therefore, in this work, the tests of alloys in the S1 and S2 solutions were carried out for 4320 hours.

Table 3. Solutions characteristics and test durations.

Solution	Composition	pH	Test duration (h)
S1	0.6 M NaCl + 0.1 M HCl	0.9	4320
S2	0.6 M NaCl + 0.1 M HCl + 10 mM H_2O_2	0.9	4320
S3	0.4 M $FeCl_3$	1.1	2352

The specimens' weights before and after the corrosion tests were recorded using the electronic balance CAUW 120D with a resolution of 0.01 mg. At least 4 samples of each alloy were subjected to the long-term corrosion tests in each solution using individual containers to ensure reproducibility. The average general corrosion rates v (mm/year) were calculated using the following equation [20]:

$$v = \frac{8.76 \cdot 10^4 \cdot W}{t \cdot A \cdot D} \quad (1)$$

where W (g) is the total weight change after the exposure time; t (h) is the immersion duration; A (cm^2) is the specimen's surface area exposed to the test solution; D is the density of the test alloy (g/cm^3). The densities D (g/cm^3) used for the calculations were the following: 8.42 for $CoCrFeNiMo_{0.4}$; 7.49 for $CoCrFeNiAl_{0.5}Cu_{0.5}$ [2, 21]; 7.94 for AISI 304, and 7.98 for AISI 316L [22].

2.3. Polarization measurements

Dimensions of the specimens were 10 mm×10 mm×5 mm for the polarization measurements. The specimens were cold-mounted in epoxy with a 1 cm^2 working area exposed to a solution. The measurements were carried out using a standard three-electrode cell. A saturated Ag/AgCl electrode was used as the reference electrode, and a platinum plate was used as the counter electrode. In this work, the potentials are reported *versus* standard hydrogen electrode (SHE). Prior to the polarization tests the specimen was immersed in the test solution, and the corrosion potential (E_{cor}) was monitored for 1 h. After that, starting from E_{cor}, the potentiodynamic curves were obtained by linear polarization technique at a potential sweep rate of 0.2 mV/s. The pitting potential (E_{pit}) and pitting basis ($\Delta E = E_{pit} - E_{cor}$) were determined from the anodic polarization curve. Each measurement was performed on independent specimens, using freshly prepared solutions at least 4 times, to ensure reproducibility.

3. Results and Discussion

3.1. Microstructure and composition characterization

SEM images of the $CoCrFeNiMo_{0.4}$ and $CoCrFeNiAl_{0.5}Cu_{0.5}$ HEAs are shown in Figure 1. The elemental analysis of the regions marked in Figure 1 is presented in Table 4. Spectra 1 and 4 correspond to the signal obtained from an area of about 1 mm^2. Spectra 2, 3, 5, and 6 correspond to the local signals obtained from particular points (the depth and diameter of interaction between the electron beam and specimens were 0.4–0.5 μm and 0.8–0.9 μm, respectively).

The alloys' actual compositions are close to the rated ones. Hypoeutectic microstructure and phase precipitates, enriched in Cr and Mo, with a size of about 10 μm were observed in $CoCrFeNiMo_{0.4}$. The relative content of this phase was significantly lower than that in CoCrFeNiMo [18]. This is due to the initially lower concentration of Mo in the $CoCrFeNiMo_{0.4}$ HEA and is explained below. It was shown [18] that the CoCrFeNiMo HEA had the hypereutectic microstructure with a high relative content of the dendritic phase enriched in Mo. The $CoCrFeNiMo_{0.4}$ matrix (dark areas in Figure 1) was less depleted in Mo. Nano-sized needle-shaped irregular particles were also observed along the edges of the bright areas.

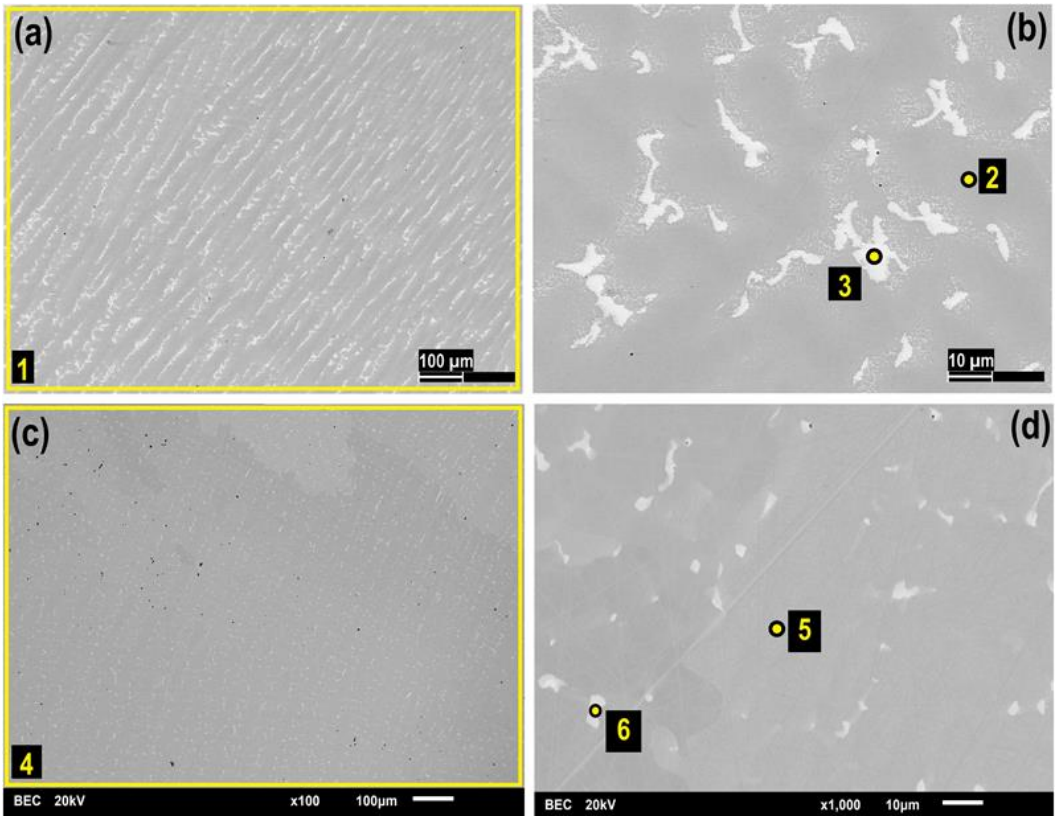

Figure 1. SEM images of the (a, b) $CoCrFeNiMo_{0.4}$ and (c, d) $CoCrFeNiAl_{0.5}Cu_{0.5}$ microstructures.

Table 4. Elemental analysis of the HEAs specimens.

Spectrum	Component's content (at.%)						
	Co	Cr	Fe	Ni	Mo	Al	Cu
1	22.6	23.3	22.2	22.8	9.1	–	–
2	23.5	22.5	23.5	23.6	6.9	–	–
3	18.4	27.7	17.7	14.4	21.8	–	–
4	20.4	21.4	20.5	20.5	–	7.1	10.1
5	21.5	22.4	21.6	20.1	–	6.5	7.9
6	5.2	4.6	5.0	13.3	–	11.7	60.2

According to the results of the EDS analysis, the total concentration of Cr and Mo in the bright phases were 50 and 51 at.% in $CoCrFeNiMo_{0.4}$ and CoCrFeNiMo [18], respectively. The sufficient contents of Mo and Cr can result in the σ-phase formation in steels and other alloys due to the number of electron holes exceeding a critical value [23, 24]. Calculating equivalent chromium content (ECC) allows one to estimate the tendency of the FCC solid solution to decompose and to predict the σ-phase formation [23]:

$$\text{ECC (wt.\%)} = [\text{Cr}] + 1.76\times[\text{Mo}] + 0.31\times[\text{Mn}] + 0.97\times[\text{W}] + 1.7\times[\text{Nb}] + 2.02\times[\text{V}] + 2.44\times[\text{Ti}] + 1.22\times[\text{Ta}] + 1.58\times[\text{Si}] - 0.177\times[\text{Co}] - 0.266\times[\text{Ni}] \quad (2)$$

where [X] is the component's content (wt.%).

If the value of ECC exceeds 17–18 wt.%, then the σ-phase is likely to appear. The ECC values, calculated from the results of the EDS analysis, were 36 and 58 wt.% for $CoCrFeNiMo_{0.4}$ and CoCrFeNiMo [18], respectively. Thus, the excess of Cr and Mo in the solid solution (dark phase) led to its supersaturation and subsequent decomposition, resulting in the σ-phase formation (bright phases) during cooling and solidification. This effect is more pronounced in CoCrFeNiMo than in $CoCrFeNiMo_{0.4}$.

Figure 2 shows the XRD peaks of the $CoCrFeNiMo_{0.4}$ and $CoCrFeNiAl_{0.5}Cu_{0.5}$ HEAs. The dark phase (spectrum 2 in Table 4) corresponds to the Ni-type FCC matrix; the bright phase (spectrum 3 in Table 4) corresponds to the σ-CrFeMo; and nano-sized needle-shaped particles at the edges of the σ-CrFeMo correspond to the μ-Co_7Mo_6. The σ- and μ-phases were indexed as the tetragonal and rhombohedral structures, respectively. The μ-phase could be formed through the σ-phase transformation by the diffusion of the atoms with a lower radius and the dislocation climb mechanism [25].

The XRD pattern of the $CoCrFeNiAl_{0.5}Cu_{0.5}$ HEA fully corresponds to the shifted spectrum of FCC Ni. It can be then concluded that the matrix exhibits the FCC solid solution structure. However, according to Figure 1 and Table 4, Cu-based phases are clearly present in the microstructure as well. Their diffraction peaks might not appear in the spectrum due to the strong texture of the specimen and/or the broadening of the main peaks. In turn, the broadening of the diffraction peaks can be attributed to the presence of crystallites of

different sizes and, if the annealing process was not sufficient in this case, to residual stresses. According to Ref. [26], the copper-containing secondary phases may be Al_2Cu and Al_4Cu_9.

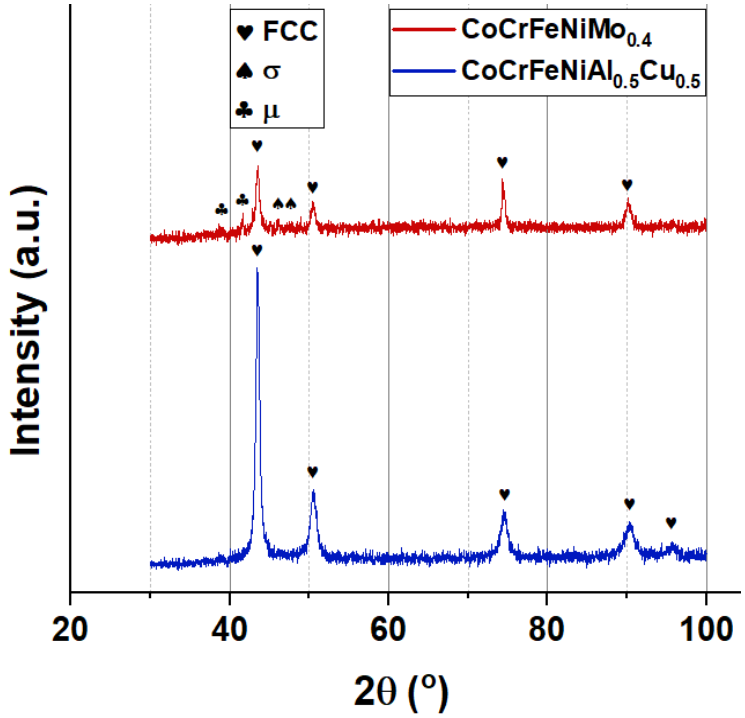

Figure 2. XRD patterns of the $CoCrFeNiMo_{0.4}$ and $CoCrFeNiAl_{0.5}Cu_{0.5}$ HEAs.

3.2. Corrosion behavior

Table 5 shows the weight losses and calculated corrosion rates of the HEAs and SSs in the S1 and S2 solutions.

Table 5. Results of the corrosion tests in the S1 and S2 solutions.

Alloy	Test solution	Weight loss (mg/cm^2)	Corrosion rate (μm/year)
$CoCrFeNiMo_{0.4}$	S1	0.5±0.2	1.3
	S2	1.46±0.07	3.5
$CoCrFeNiAl_{0.5}Cu_{0.5}$	S1	14.6±1.6	40
	S2	81.32±0.14	220
AISI 304	S1	0.20±0.05	0.5
	S2	0.48±0.01	1.23
AISI 316L	S1	0.40±0.04	1.0
	S2	0.49±0.01	1.26

The corrosion rates of CoCrFeNiMo [18], $CoCrFeNiMo_{0.4}$, SS 304, and SS 316L were not higher than 3 μm/year in the acidic NaCl solution. Nevertheless, it can be seen that the corrosion rates of the molybdenum-containing HEAs and SS 316L were higher compared to the SS 304. Indeed, if the Cr concentration is insufficient, adding molybdenum to the Fe-Cr-Ni alloys becomes less effective or even detrimental to their corrosion resistance in acidic chloride solutions [27, 28]. Thus, the higher corrosion rates of the molybdenum-containing alloys compared to the SS 304 may be due to the lower Cr content (CoCrFeNiMo, SS 316L) and uneven distribution of Cr and Mo (CoCrFeNiMo, $CoCrFeNiMo_{0.4}$). The latter leads to a situation where the potential ennoblement occurs non-uniformly over the surface. As a result, in the case of molybdenum-containing HEAs, the σ-phase and matrix form a microgalvanic couple. This effect may manifest itself mainly during the initial stages of corrosion, before the stabilization of a stationary passive state. The corrosion rate of the $CoCrFeNiAl_{0.5}Cu_{0.5}$ HEA in the S1 solution was approximately 40 μm/year. The corrosion rate of CoCrFeNiMo increased by an order of magnitude (from 1 to 21 μm/year) in the presence of 10 mM H_2O_2 [18]. The corrosion rates of $CoCrFeNiMo_{0.4}$ and SSs in the S2 solution were not higher than 5 μm/year. The corrosion rate of $CoCrFeNiAl_{0.5}Cu_{0.5}$ increased by 5.5 times with the addition of 10 mM H_2O_2.

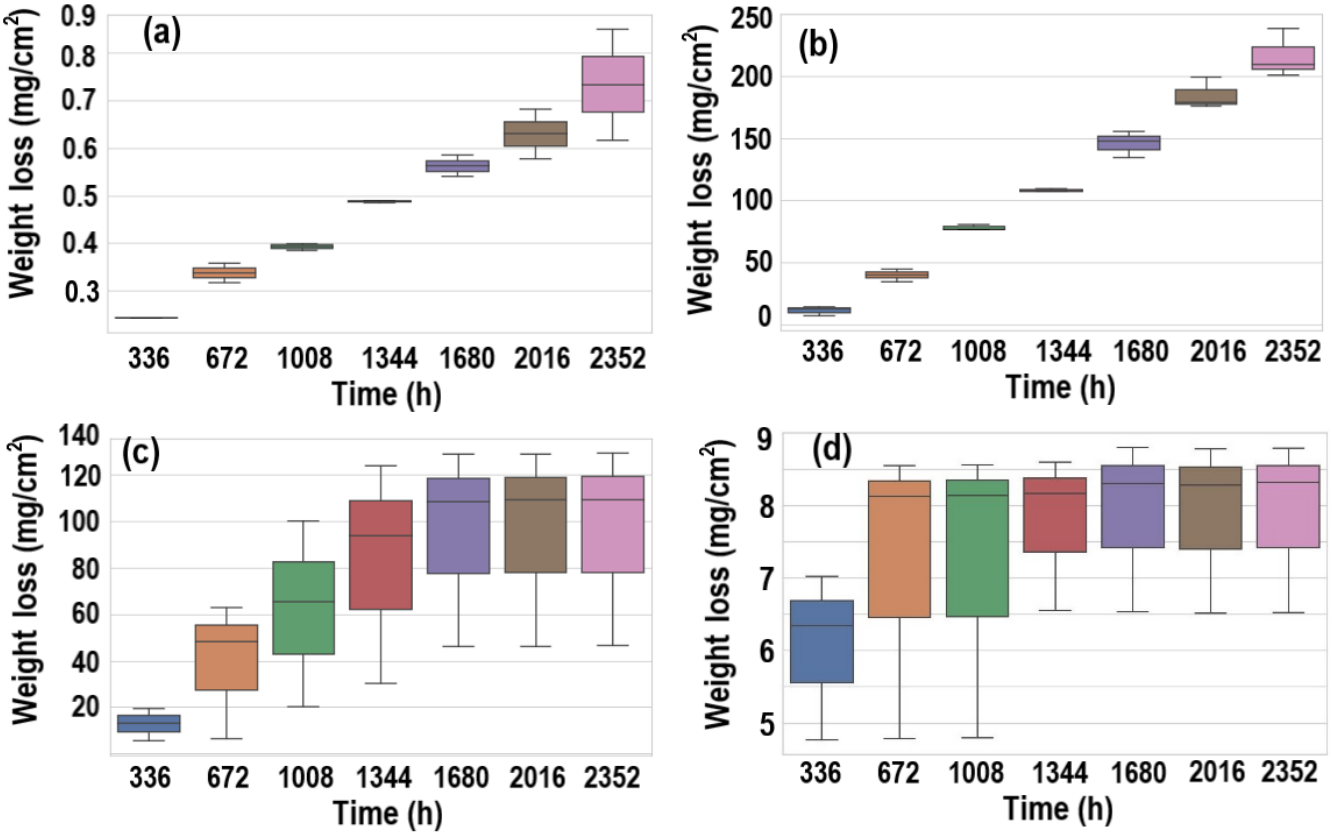

Figure 3. Weight losses of the (a) $CoCrFeNiMo_{0.4}$, (b) $CoCrFeNiAl_{0.5}Cu_{0.5}$, (c) SS 304, and (d) SS 316L alloys during the corrosion tests in the S3 solution.

Figure 3 shows the HEAs and SSs weight losses in the S3 solution. The lower and upper boundaries of the rectangles correspond to the 25th and 75th percentiles, respectively. The line inside the rectangle corresponds to the 50th percentile (median). The lower and upper horizontal lines of the "whiskers" represent the minimum and maximum measurement values, respectively. The corrosion rates, calculated *via* equation (1), are presented in Figure 4a.

The weight loss of $CoCrFeNiMo_{0.4}$ increased up to 0.75 mg/cm^2 over time. However, it can be seen in Figure 4a that the corrosion rate gradually decreased over time, with the average corrosion rate (over the entire test period of 2352 h) being just 3 μm/year. The highest corrosion rate of the $CoCrFeNiMo_{0.4}$ HEA (8 μm/year) was observed during the initial period up to 336 h. The weight loss and corrosion rate of $CoCrFeNiAl_{0.5}Cu_{0.5}$ steadily increased and reached the values of 207 mg/cm^2 and 1.08 mm/year, respectively.

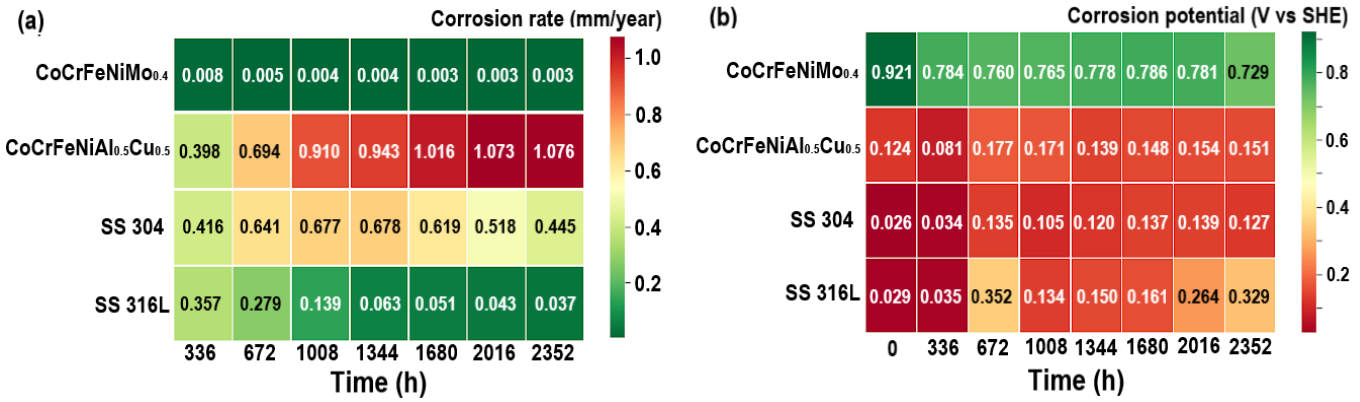

Figure 4. Heatmaps of the (a) average corrosion rates and (b) corrosion potential changes.

The test results for the SS 304 have a significant spread of the data (Figure 3c). However, from the average values of the corrosion rates, it is clear that the most rapid increase in corrosion rate occurred during the first 672 h of testing (Figure 4a). Then the growth slowed down, after which the corrosion rate decreased and reached a constant value of 0.4–0.5 mm/year. In the case of the SS 316L, there is also a scatter in the experimental data (Figure 3d). Similar to $CoCrFeNiMo_{0.4}$, the maximum corrosion rate of the SS 316L was reached during the first 336 h of testing, after which it decreased and further reached a constant value (Figure 4a). The values of weight losses and corrosion rates of the SS 316L are an order of magnitude lower than those of SS 304. Thus, the time for the corrosion rate to increase to its peak value in the S3 solution was longer in the case of the SS 304 compared to the molybdenum-containing $CoCrFeNiMo_{0.4}$ and SS 316L alloys. Accordingly, molybdenum, when present in the alloy in moderate amounts, is beneficial to the long-term corrosion resistance in chloride oxidizing solutions. At the same time, the corrosion rate of the $CoCrFeNiMo_{0.4}$ HEA in the S3 solution was lower compared to that of the SS 316L.

Since the highest corrosion rates were expected in the S3 solution, the corrosion potentials were also measured during the specimens' exposure to this environment (Figure 4b). The most negative corrosion potential values corresponded to the highest

corrosion rates ($CoCrFeNiAl_{0.5}Cu_{0.5}$ and SS 304). The corrosion potentials' changes and the corrosion rates' changes were consistent with each other – the significant potential shifts in a positive direction characterized time intervals in which there was a considerable deceleration in the growth of the corrosion rate or its decrease. After 336–672 h of testing, the corrosion potentials of all alloys, except SS 316L, stabilized and subsequently remained close to the stationary values. The corrosion potential of the SS 316L shifted towards both more positive and more negative values, which may indicate transitions between active and passive states of the surface.

3.3. Surface analysis after corrosion tests

The studies were carried out on the specimens tested in the S2 and S3 solutions, since the weight losses and, accordingly, the corrosion rates of the alloys were the most significant in these solutions. SEM images of the $CoCrFeNiMo_{0.4}$ surfaces before and after the corrosion tests in the S2 and S3 solutions are presented in Figure 5. In the matrix regions proximate to the σ-phase, the traces of corrosion were observed in the form of pits with a diameter of less than 1 μm. The σ-phase itself and the matrix regions remote from it remained practically undamaged. It was shown in Ref. [18] that the entire Mo-depleted matrix was mainly corroded during the exposure of the CoCrFeNiMo HEA to the S2 and S3 solutions. However, the Mo-enriched areas (σ-phase) also lost their corrosion resistance over time. The overall surface damage of the $CoCrFeNiMo_{0.4}$ HEA was significantly lower than that of CoCrFeNiMo.

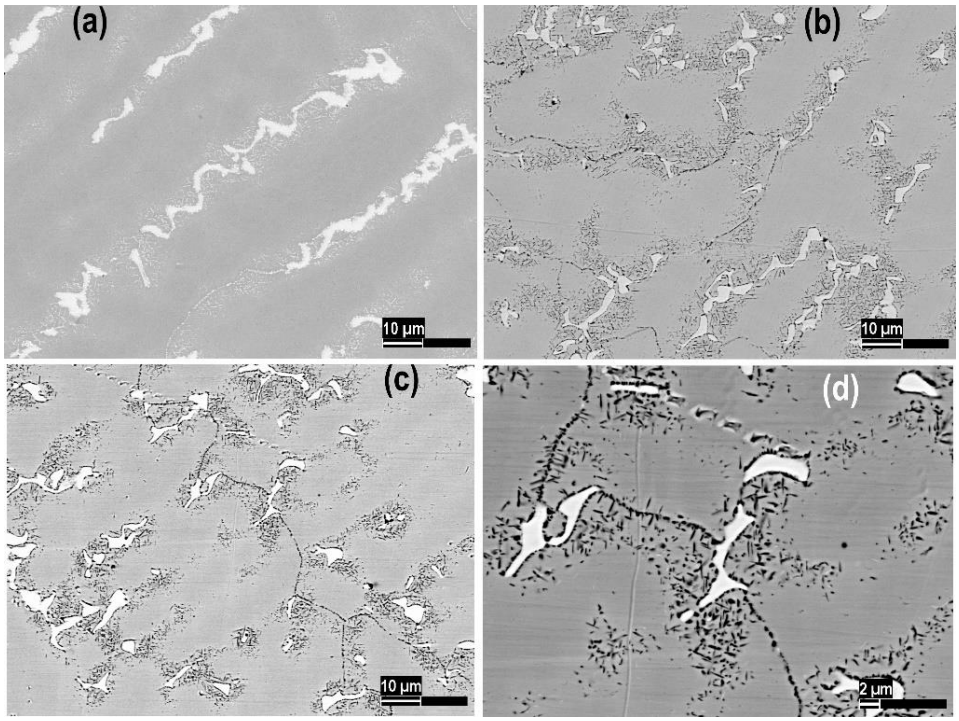

Figure 5. SEM images of the $CoCrFeNiMo_{0.4}$ surface morphologies (a) before and (b–d) after the corrosion tests in the (b) S2 and (c, d) S3 solutions.

Figure 6 shows the EDS mapping results of the $CoCrFeNiMo_{0.4}$ HEA after the corrosion tests in the S2 and S3 solutions. The results of elemental analysis of the surfaces before and after testing coincided within the measurement error of the device. Thus, in this case, the sensitivity of the EDS method turned out to be insufficient to detect changes in the composition of the $CoCrFeNiMo_{0.4}$ surface.

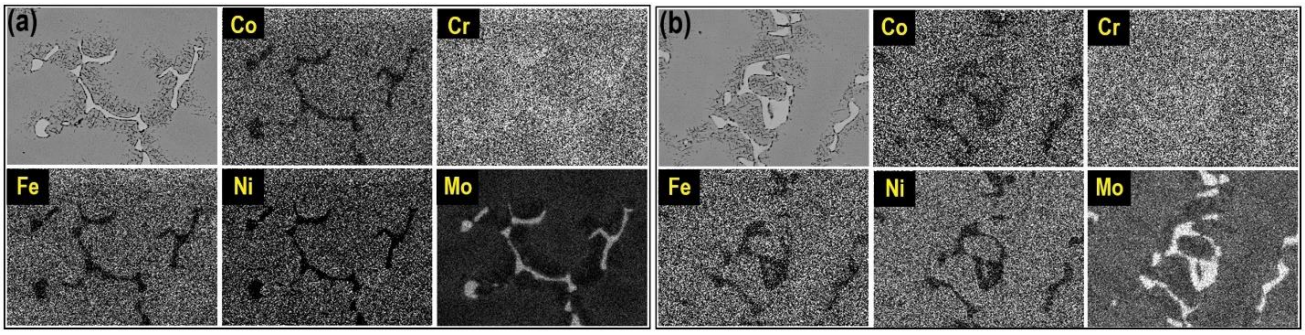

Figure 6. EDS maps of the $CoCrFeNiMo_{0.4}$ surface after the corrosion tests in the (a) S2 and (b) S3 solutions.

The results of the $CoCrFeNiMo_{0.4}$ surface analysis did not show the presence of corrosion products on it. It should be noted that on the map of molybdenum distribution the areas of pit formation appeared darker compared not only to the σ-phase but also to the matrix areas without corrosion defects (Figure 6a). Thus, the damaged matrix regions proximate to the σ-phase were depleted with molybdenum compared to the undamaged matrix regions distant from the σ-phase and subsequently unaffected by corrosion. It is likely that the local passive films, formed on the matrix areas proximate to the boundaries with the σ-phase, had a lower protective ability due to the lower Mo content. For the same reason, these regions could be anodic to both σ-phase and matrix regions with a higher Mo content.

SEM images of the $CoCrFeNiAl_{0.5}Cu_{0.5}$ surfaces before and after the corrosion tests in the S2 and S3 solutions are presented in Figure 7.

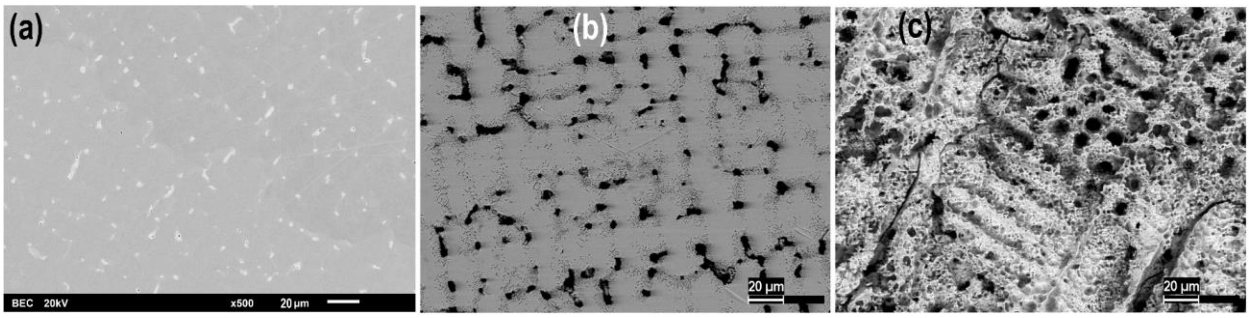

Figure 7. SEM images of the $CoCrFeNiAl_{0.5}Cu_{0.5}$ surface morphologies (a) before and (b, c) after the corrosion tests in the (b) S2 and (c) S3 solutions.

Numerous pits of 8–10 μm in size were observed on the surface $CoCrFeNiAl_{0.5}Cu_{0.5}$ after the corrosion tests in the S2 solution. The defects tended to coalesce during their growth (Figure 7b). The alloy surface was particularly damaged due to corrosion in the S3 solution.

Crack-like defects were also visible along with the many large pits (Figure 7c). Figure 8 shows the EDS mapping results of the $CoCrFeNiAl_{0.5}Cu_{0.5}$ HEA after the corrosion tests in the S2 and S3 solutions. The results of the corresponding elemental analysis in single regions are presented in Figure 9. During the analysis of the pits formed in the S3 solution, significant signal distortions occurred due to the large depth of the defects. For this reason, the analysis results are only shown for the area presented in Figure 8b.

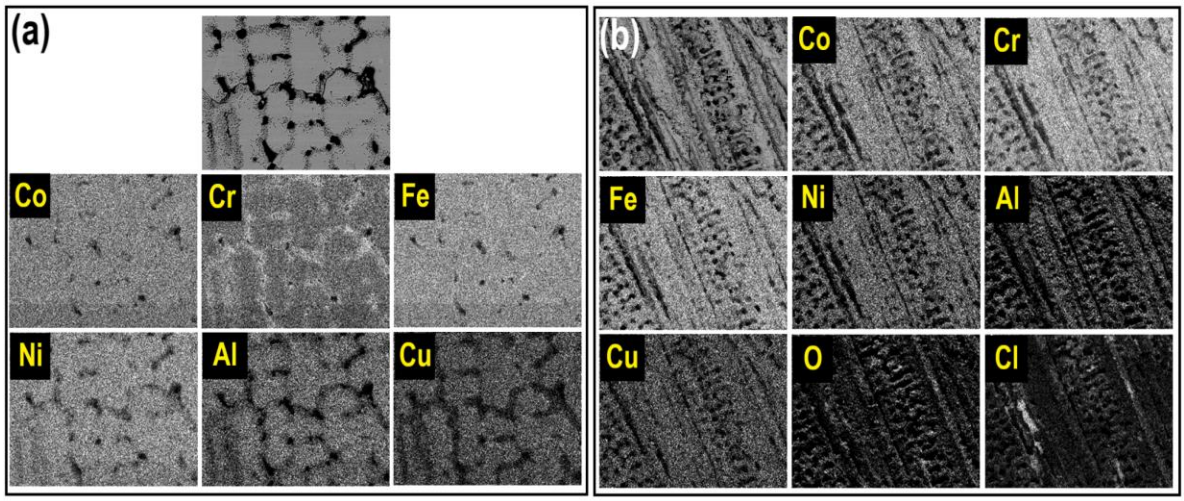

Figure 8. EDS maps of the $CoCrFeNiAl_{0.5}Cu_{0.5}$ surface after the corrosion tests in the (a) S2 and (b) S3 solutions.

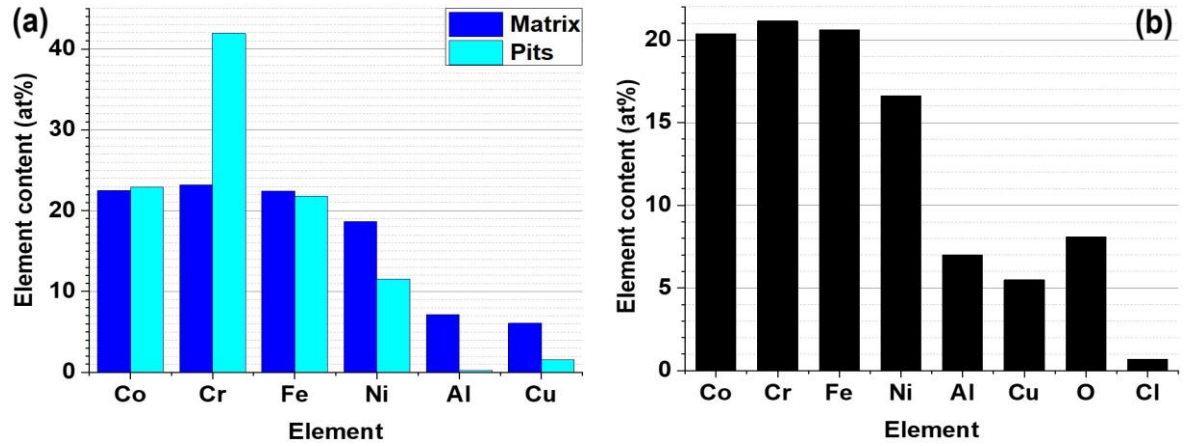

Figure 9. Elemental analysis of the $CoCrFeNiAl_{0.5}Cu_{0.5}$ surface after the corrosion tests in the (a) S2 and (b) S3 solutions.

During the corrosion process in the S2 solution, aluminum and copper dissolved to a greater extent than all the other elements included in the $CoCrFeNiAl_{0.5}Cu_{0.5}$ composition. Not only the pits were significantly depleted with Al and Cu but also the areas between them (Figure 8a). It is worth noting that the surface areas, depleted with aluminum and copper, became enriched with chromium at the same time. It is likely that the presence of Al and Cu in corrosion products substantially decreased the stability and protective ability of the Cr-

based passive layer [29]. As a result, the active local corrosion occurred on the $CoCrFeNiAl_{0.5}Cu_{0.5}$ surface. The dissolution process was presumably initiated at the locations of the Cu-based precipitates. According to the elemental analysis results, oxygen- and chlorine-containing (8 and 1 at.%, respectively) corrosion products were detected in the case of S3 solution (Figure 9b).

The SS 304 underwent both pitting and intergranular corrosion in the presence of 10 mM H_2O_2, which is clearly visible in Figure 10a. The corrosion process was so intense in the S3 solution that it led to macroscopic changes in the surface topography. For this reason, studying the morphology using SEM seemed impractical in this case. On the surface of the 316L steel after the corrosion tests in the S2 and S3 solutions, signs of dissolution along the grain boundaries are also clearly visible, as well as the pits with sizes less than 1 μm in the S2 solution (Figure 10b) and less than 2 μm in the S3 solution (Figure 10c).

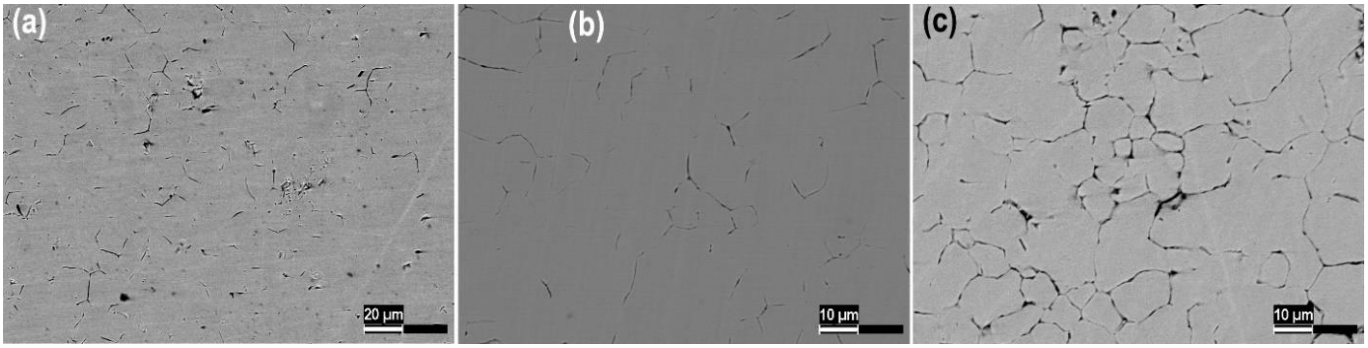

Figure 10. Signs of pitting and intergranular corrosion of the (a) SS 304 in the S2 solution and (b, c) SS 316L in the (b) S2 and (c) S3 solutions.

3.4. Electrochemical measurements

The variation in corrosion potentials during 1 h exposure to the test solutions is shown in Figure 11. The corrosion potentials of the $CoCrFeNiMo_{0.4}$ and $CoCrFeNiAl_{0.5}Cu_{0.5}$ HEAs changed slightly in the S1 solution (Figure 11a). In the case of CoCrFeNiMo and SS 316L, the E_{cor} values shifted in a positive direction, while E_{cor} of the SS 304, on the contrary, shifted to more negative values over time (Figure 11a). In the S2 solution with the oxygen-containing oxidizer (10 mM H_2O_2), only E_{cor} of the CoCrFeNiMo HEA shifted in a positive direction (Figure 11b). However, the shift value was less than that in the S1 solution. For all the other alloys, E_{cor} shifted to more negative values over time. Moreover, in the case of the SSs 304 and 316L, sharp fluctuations in the potential values were detected during the specimens' exposure to the S2 solution. In the S3 solution with the cationic oxidizer (Figure 11c), the positive shift in the $CoCrFeNiMo_{0.4}$ E_{cor} along with the rapid steps in a negative direction, the stable E_{cor} values of the CoCrFeNiMo и $CoCrFeNiAl_{0.5}Cu_{0.5}$ HEAs, and the E_{cor} shifts in a negative direction for the SSs 304 and 316L were observed. Moreover, noticeable potential fluctuations in the case of the SS 316L were recorded. When the type of the oxidizer changed and its content increased, the corrosion potentials of all the HEAs became more positive. The largest shifts were observed in the case of $CoCrFeNiMo_{0.4}$. For

SSs, on the contrary, there was no potential shift between the S2 and S3 solutions, which might indicate the ongoing local corrosion process.

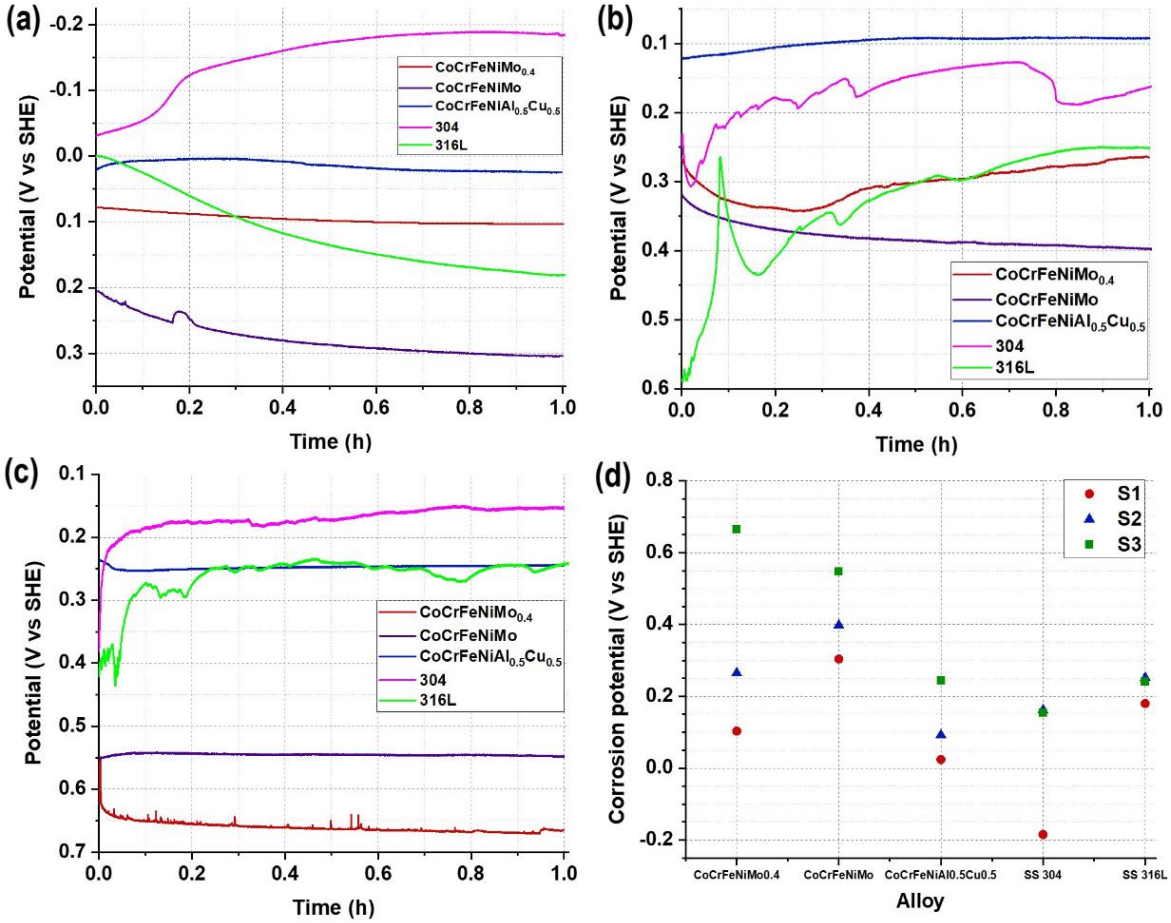

Figure 11. Changes of the HEAs and SSs corrosion potentials in the (a) S1, (b) S2, and (c) S3 solutions and (d) the values after 1 h exposure.

Figure 12 depicts the anodic polarization curves of the HEAs and SSs. The anodic curve of SS 304 had distinctive regions of active dissolution, active-passive transition, passivation, and local dissolution in the S1 solution. In the same solution the anodic curves of the molybdenum-containing alloys $CoCrFeNiMo_{0.4}$, CoCrFeNiMo, and SS 316L demonstrated passive regions, in which the current density increased slightly or did not change with increasing external anodic polarization, as well as a region of passivity breakdown caused by the local dissolution of the electrode. The pitting potential of the $CoCrFeNiMo_{0.4}$ HEA was more positive by 680 and 900 mV than those of the SSs 316L and 304, respectively (Figure 12a). However, the current density in the passive region was 4–5 μA/cm^2. This value was several times higher than the corresponding parameters of the SSs 304 and 316L, which is consistent with the higher $CoCrFeNiMo_{0.4}$ corrosion rate in the S1 solution. A gradual increase in the dissolution current and the absence of a passive region in the S1 solution were observed on the anodic curve of the molybdenum-free $CoCrFeNiAl_{0.5}Cu_{0.5}$ HEA. The presence of the oxygen-containing oxidizer (10 mM H_2O_2) in the S2 solution led

to the absence of the passive regions of all the alloys except $CoCrFeNiMo_{0.4}$. Its pitting basis decreased by approximately 1.2 times in this case (Figure 13b). Nevertheless, this occurred mainly due to the shift of E_{cor} to more positive values rather than to a decrease in the pitting potential (Figure 13a).

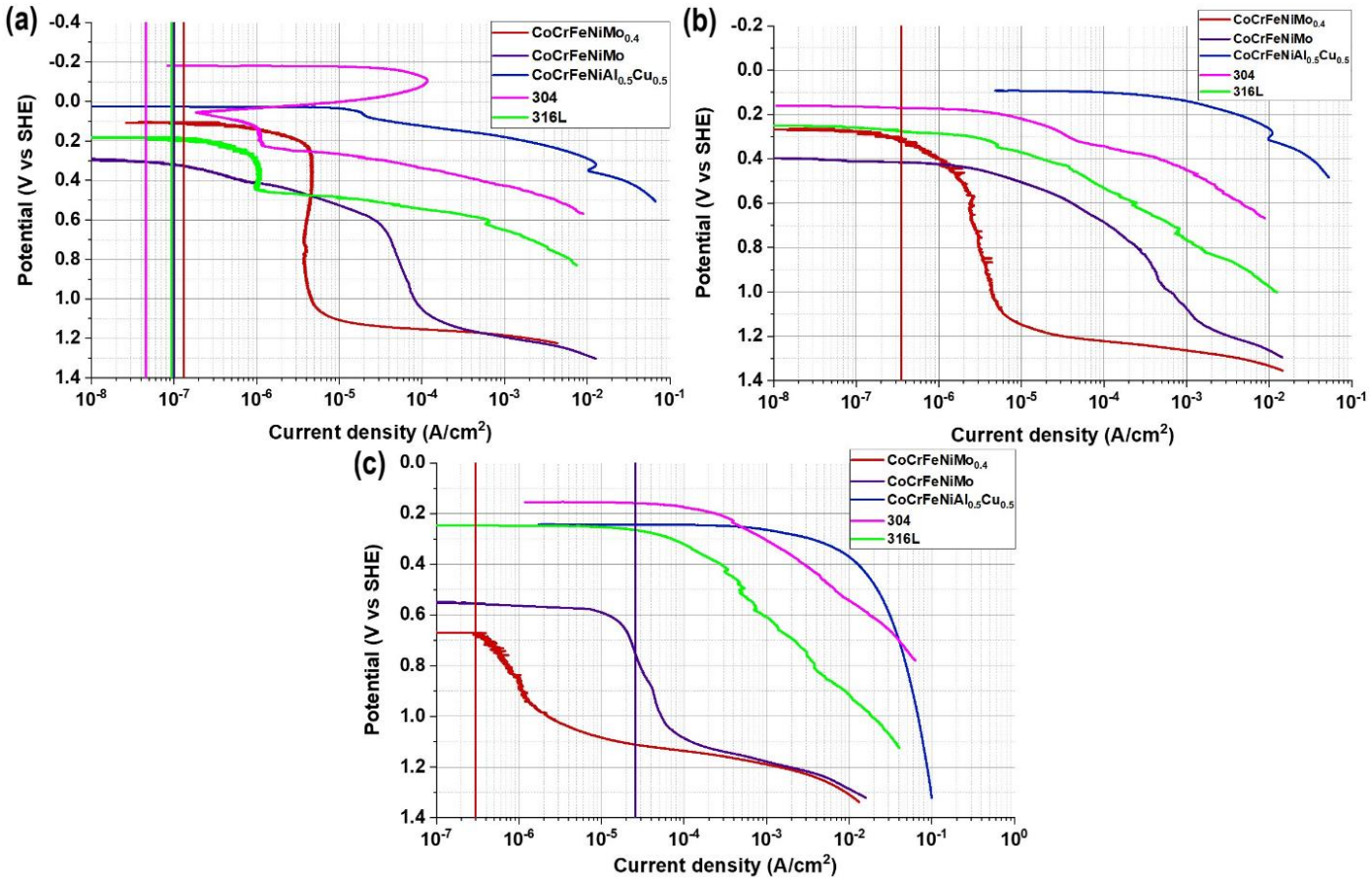

Figure 12. Anodic polarization curves of the HEAs and SSs in the (a) S1, (b) S2, and (c) S3 solutions. Vertical lines represent the corrosion current densities calculated from the corrosion rates.

The SSs were not passivated in the S3 solution, either (Figure 12c). The $CoCrFeNiMo_{0.4}$ HEA exhibited an even greater decrease in the pitting basis (Figure 13b), but the current density in the passive region did not exceed 1 μA/cm^2 (Figure 12c). The pitting basis of the CoCrFeNiMo HEA turned out to be 2 times greater than that of $CoCrFeNiMo_{0.4}$ (Figure 13b). However, the current density in the passive region of CoCrFeNiMo reached 50 μA/cm^2 (Figure 12c).

Thus, the presence of an oxidizing agent and an increase in the concentration of chloride ions had a slight effect on the pitting potentials of the molybdenum-containing HEAs (Figure 13a). This fact may indicate high resistance to the local corrosion. Due to the significant shift of E_{cor} in a positive direction in the S2 and S3 solutions, the HEAs pitting bases decreased.

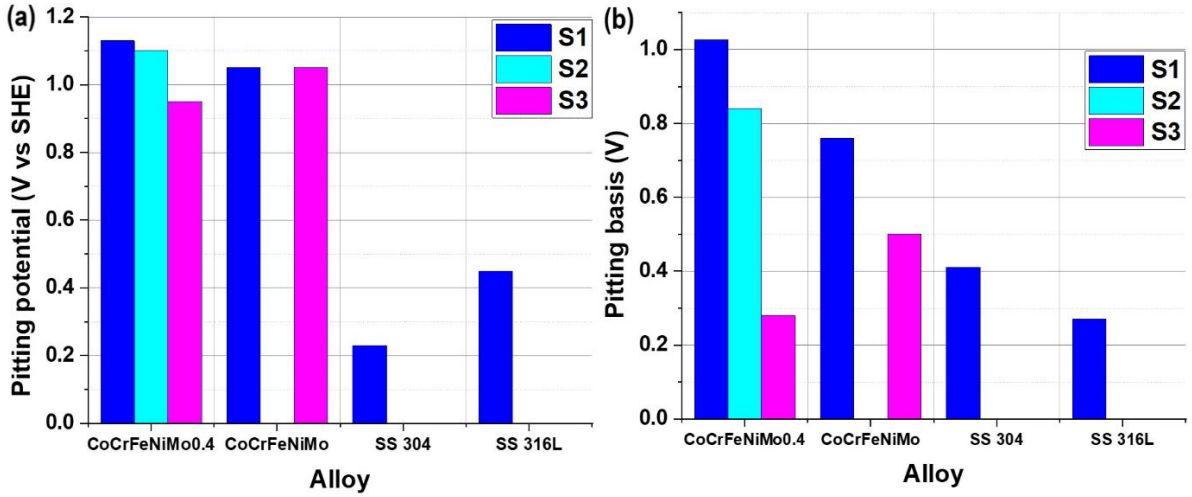

Figure 13. (a) Pitting potentials and (b) pitting bases.

Current density fluctuations were visible on the $CoCrFeNiMo_{0.4}$ anodic polarization curves, which may be associated with the generation of metastable pits and explain the weight losses of this HEA during the long-term corrosion tests. According to the SSs 304 and 316L polarization curves obtained in the S2 and S3 solutions, the positive effect of molybdenum was noticeable and pronounced despite the absence of the passive regions. Mo inhibits the dissolution of the steel in the active state [30, 31], which explains the higher long-term corrosion resistance of the SS 316L in the oxidizing chloride solutions compared to the SS 304. Passive films of austenitic corrosion-resistant molybdenum-containing steels [32–34] and nickel alloys [35–37] exhibit a bilayer structure. In the inner layer, defective areas, locally enriched in iron oxide and depleted in chromium oxide, are prone to the initiation and propagation of corrosion damage in them [38]. However, molybdenum effectively prevents passivity breakdown. In Refs. [38–40], the mechanism of it is investigated in detail and thoroughly described in terms of mitigating the penetration of chloride ions, blocking their ingress to the defective sites, supressing the formation of oxygen vacancies in the oxides, and intensifying the selective dissolution of Fe followed by the substitution of iron with chromium and molybdenum in the inner layer. Thus, the concentration of Mo in $CoCrFeNiMo_{0.4}$ resulted in such contents of Cr and Mo in the matrix and σ-phase that the distribution of these elements between the phases effectively hindered passivity breakdown and selective corrosion.

For the alloy-solution combinations, in which the passive regions were observed on the anodic polarization curves (Figure 12), in accordance with equation (3), the corrosion current density was calculated based on the corrosion rates determined from the gravimetric tests:

$$i_{cor} = \frac{v \cdot D}{3.27 \cdot 10^{-3} \cdot EW} \quad (3)$$

where i_{cor} is the corrosion current density ($\mu A/cm^2$);

$EW = \frac{1}{\sum_{i} \frac{n_i f_i}{W_i}}$ is the alloy's equivalent weight: n_i is the valence of the i^{th} element in the alloy; f_i is the mass fraction of the i^{th} element in the alloy; W_i is the atomic weight of the i^{th} element in the alloy.

The value of *n* was taken equal to 2 for Co, Fe, and Ni; 3 for Cr and Mo [41, 42]. For the HEAs, the values of *f* were determined by converting the results of elemental analysis (Table 4) into mass fractions, and the values corresponding to the rated compositions were used for steels (Table 2). The calculated corrosion current densities are shown by vertical lines in Figure 12. It can be seen that, in the S1 and S2 solutions, the corrosion current densities of the molybdenum-containing HEAs and SSs 304 and 316L were significantly less than the current densities in their passive regions. This is due to the fact that the stationary passive state is established over time during the long-term corrosion tests. This state is characterized by a substantially lower current density compared to the values achieved during the polarization measurements after the stabilization of the corrosion potential for 1 hour. Additionally, the changes in corrosion rates over time should be considered. The method based on obtaining the polarization curves allows one to determine the instantaneous corrosion rate, and the gravimetric method – the corrosion rate averaged over a long time. However, the calculated corrosion current densities of the molybdenum-containing HEAs in the S3 solution are consistent with the values in their passive regions on the obtained polarization curves. The possible discrepancies between the quantitative results of gravimetric and electrochemical tests in terms of corrosion resistance should be taken into account when predicting the alloys' long-term behavior and justifying their industrial applications.

3.5. Surface analysis after potentiodynamic anodic polarization

SEM images of the $CoCrFeNiMo_{0.4}$ surfaces before and after the polarization measurements in the S2 and S3 solutions are depicted in Figure 14. The surface area covered by the σ-phase turned out to be larger after the electrochemical measurements than in the initial state. This indicates the preferential dissolution of the matrix. Near the interface between the σ-phase and the matrix, numerous local defects with a diameter of less than 1 μm were visible in the matrix (Figure 14c and Figure 14e). In the σ-phase, there also were areas clearly affected by the dissolution in the S3 solution.

Figure 15 shows the EDS mapping results of the $CoCrFeNiMo_{0.4}$ HEA after the potentiodynamic polarization in the S2 and S3 solutions. The results of the corresponding elemental analysis in single regions are presented in Figure 16.

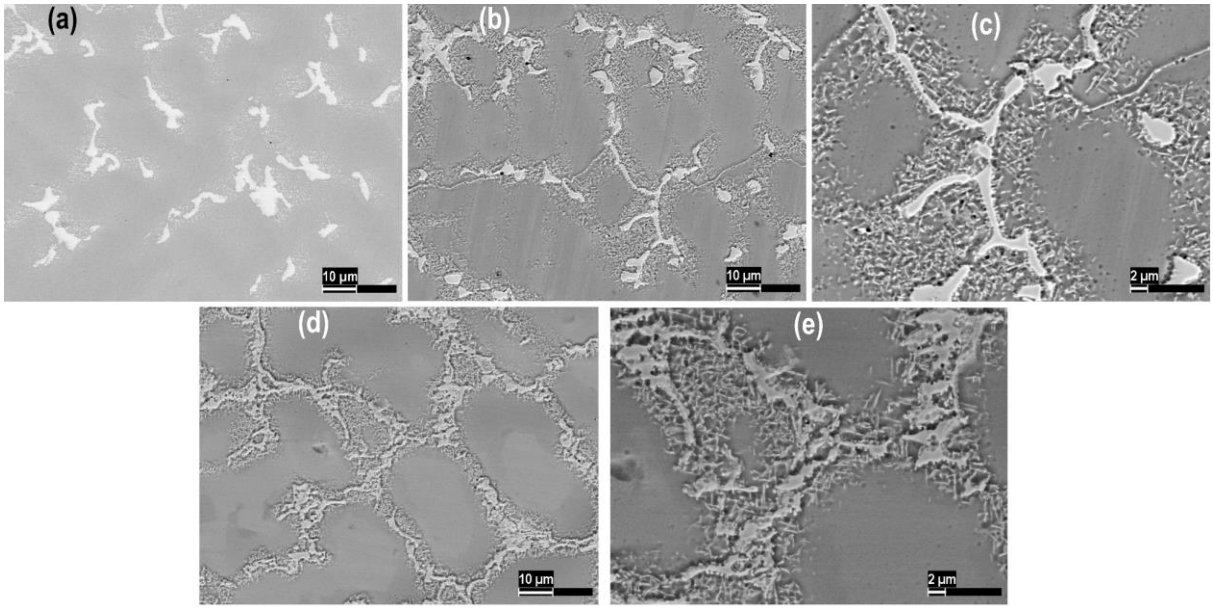

Figure 14. SEM images of the $CoCrFeNiMo_{0.4}$ surfaces morphologies (a) before and (b–e) after the potentiodynamic polarization in the (b, c) S2 and (d, e) S3 solutions.

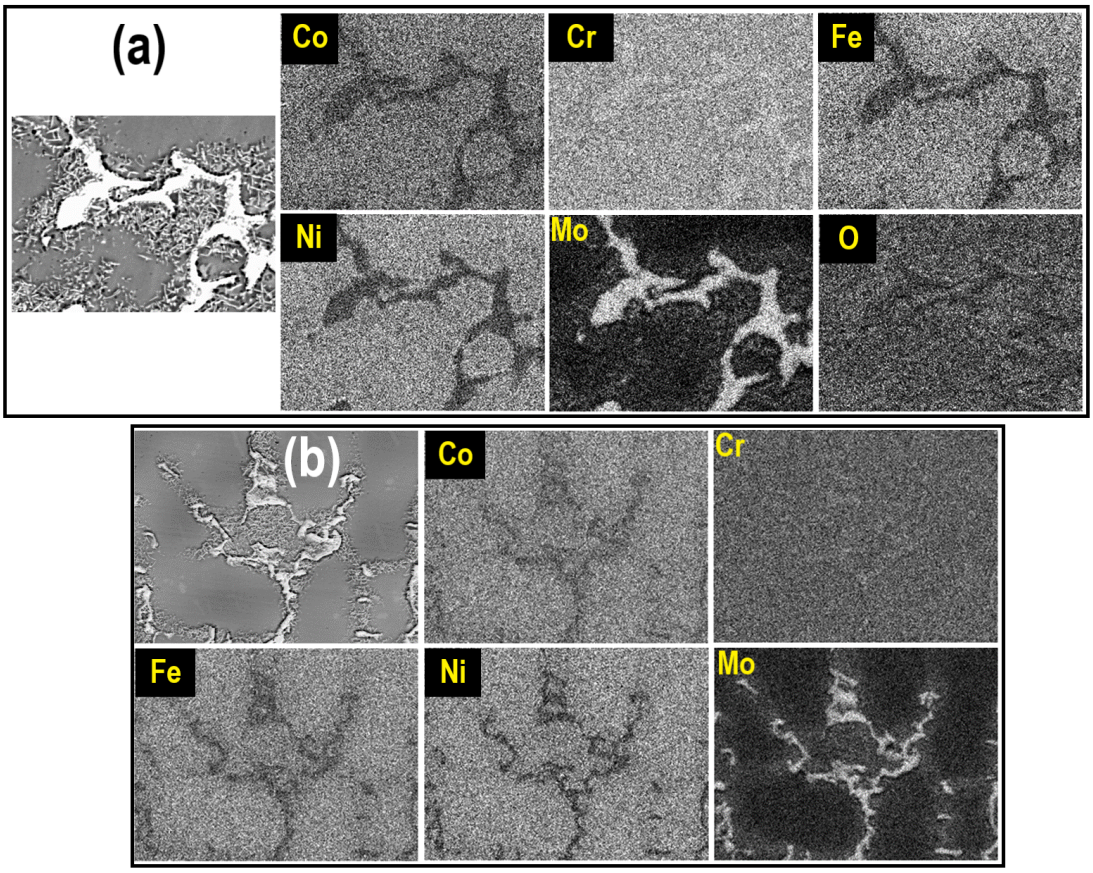

Figure 15. EDS maps of the $CoCrFeNiMo_{0.4}$ surface after the potentiodynamic polarization in the (a) S2 and (b) S3 solutions.

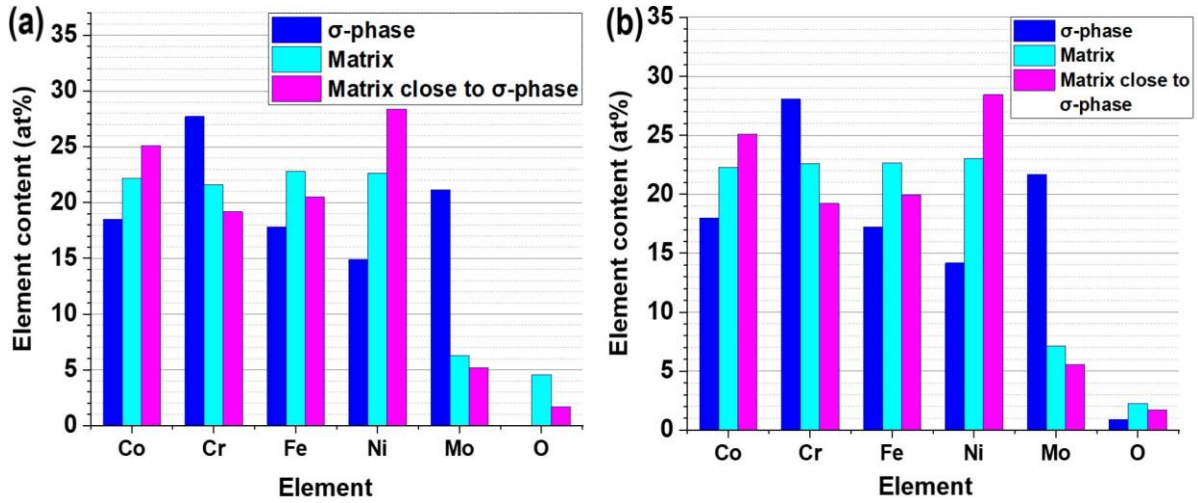

Figure 16. Elemental analysis of the $CoCrFeNiMo_{0.4}$ surface after the potentiodynamic polarization in the (a) S2 and (b) S3 solutions.

The presence of the corrosion products with an oxygen content of up to 5 at.% (S2 solution) and up to 3 at.% (S3 solution) was revealed at the locations of the matrix. The most damaged areas of the matrix located close to the σ-phase became enriched with nickel as a result of the alloy's anodic dissolution. The depth of interaction between the electron beam and the alloy was 0.4–0.5 μm, and the typical thickness of the passive films on the HEAs and stainless steels is several nm [6, 43, 44]. Therefore, the results of elemental analysis were obtained using the signal from both corrosion products and modified surface layers of the alloy. Thus, nickel enrichment can be explained by analogy with the behavior of austenitic stainless steels. During the formation of a passive film, the modified layer of an alloy's surface becomes enriched with nickel due to the preferential oxidation of Fe and Cr at the metal/oxide interface in comparison with Ni [45].

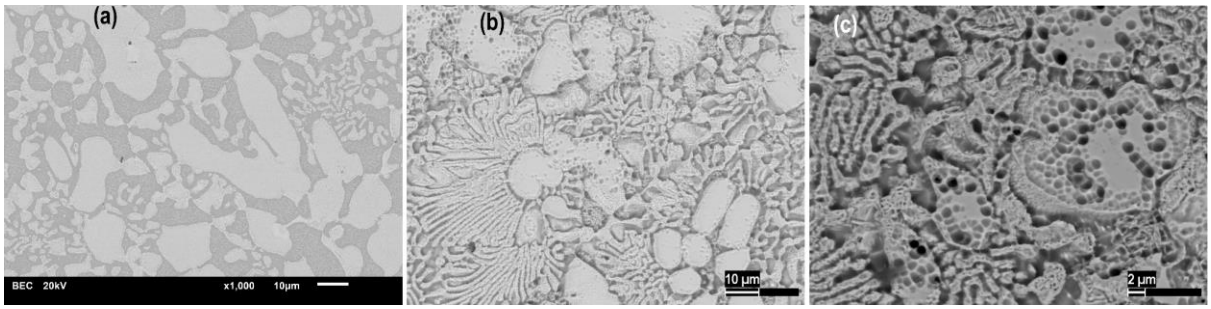

Figure 17. SEM images of the CoCrFeNiMo surface morphologies (a) before and (b, c) after the potentiodynamic polarization in the S3 solution.

SEM images of the CoCrFeNiMo surfaces before and after the polarization measurements in the S3 solution are depicted in Figure 17. The dissolution of the molybdenum-depleted matrix occurred most intensively. However, the Mo-rich σ-phase was also damaged. Numerous pits with a diameter of 1–2 μm were observed. The defects coalesced, which can be interpreted as a pseudo-uniform dissolution of the dendritic phase.

The overall damage degree of the CoCrFeNiMo surface was significantly higher than that of the $CoCrFeNiMo_{0.4}$ HEA.

After the potentiodynamic anodic polarization of the CoCrFeNiMo HEA in the S2 solution, the presence of corrosion products with an oxygen content of up to 40 at.% at the locations of the alloy matrix was shown [18]. Figure 18 depicts the EDS mapping results of the CoCrFeNiMo HEA after the potentiodynamic polarization in the S3 solution. The results of the corresponding elemental analysis in single regions are shown in Figure 19. The regions of the local defects in the σ-phase were depleted with Mo compared to the undamaged σ-phase areas.

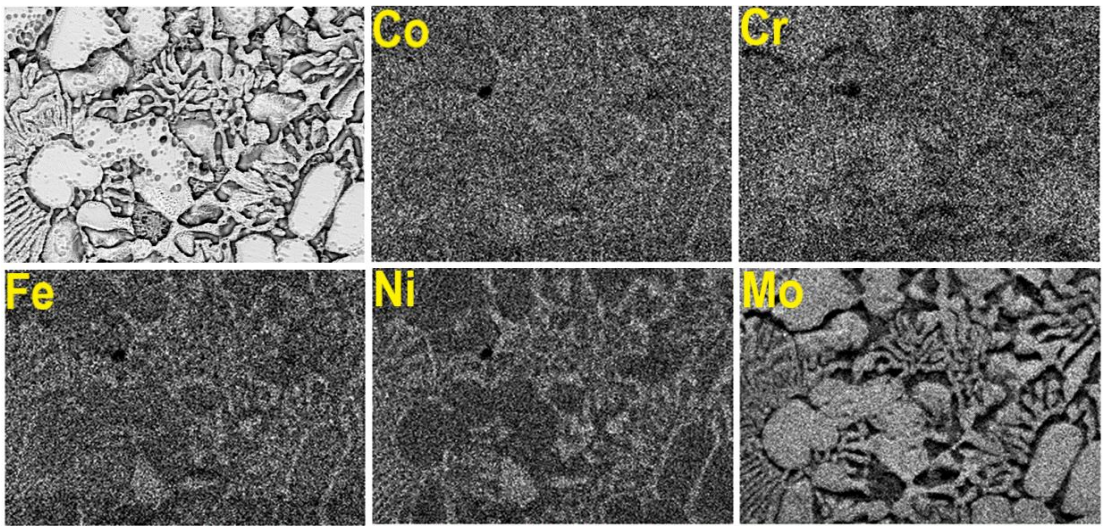

Figure 18. EDS maps of the CoCrFeNiMo surface after the potentiodynamic polarization in the S3 solution.

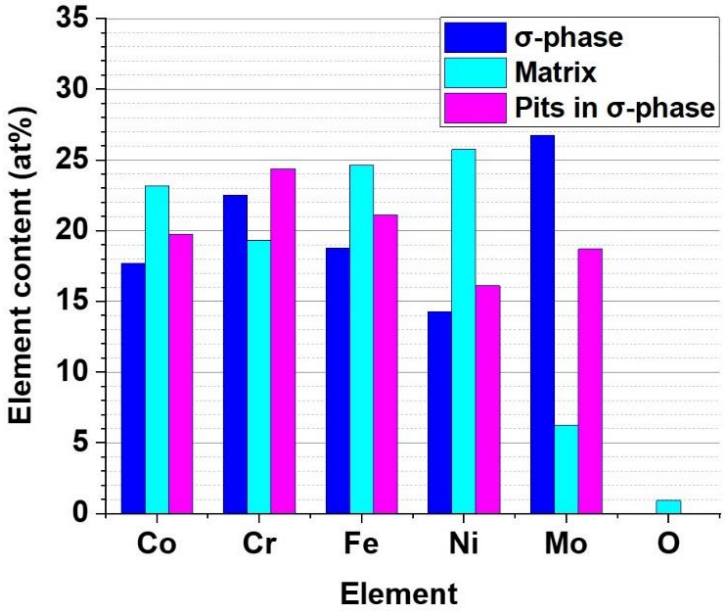

Figure 19. Elemental analysis of the CoCrFeNiMo surface after the potentiodynamic polarization in the S3 solution.

SEM images of the $CoCrFeNiAl_{0.5}Cu_{0.5}$ surfaces before and after the polarization measurements in the S2 and S3 solutions are presented in Figure 20.

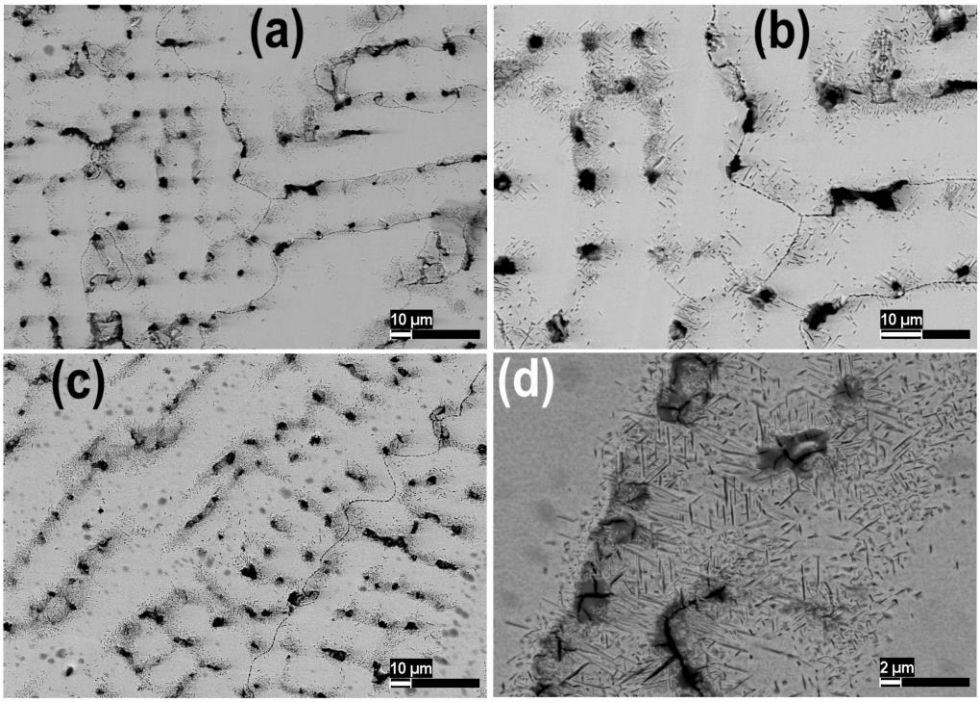

Figure 20. SEM images of the $CoCrFeNiAl_{0.5}Cu_{0.5}$ surfaces morphologies after the potentiodynamic polarization in the (a, b) S2 and (c, d) S3 solutions.

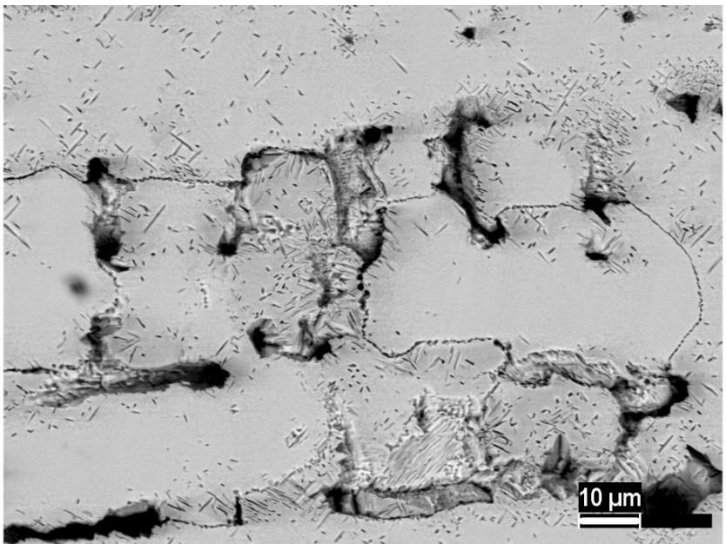

Figure 21. Pits coalescence and crack-like defects formation on the $CoCrFeNiAl_{0.5}Cu_{0.5}$ surface as a result of the potentiodynamic polarization in the S2 solution.

The HEA underwent the local dissolution process as a result of the potentiodynamic anodic polarization. Numerous pits of up to 8 μm in size were discovered. In some places on the surface, the cracking of corrosion products was noticeable (Figure 20d), which indicated

their low protective ability. The local defects tended to coalesce during propagation. It led to the formation of crack-like defects on the surface (Figure 21). This effect may be associated with residual stresses if the annealing process (900°C/1 h) was not sufficient in this case.

Figure 22 depicts the EDS mapping results of the $CoCrFeNiAl_{0.5}Cu_{0.5}$ HEA after the potentiodynamic polarization in the S2 and S3 solutions. The results of the corresponding elemental analysis in single regions are shown in Figure 23.

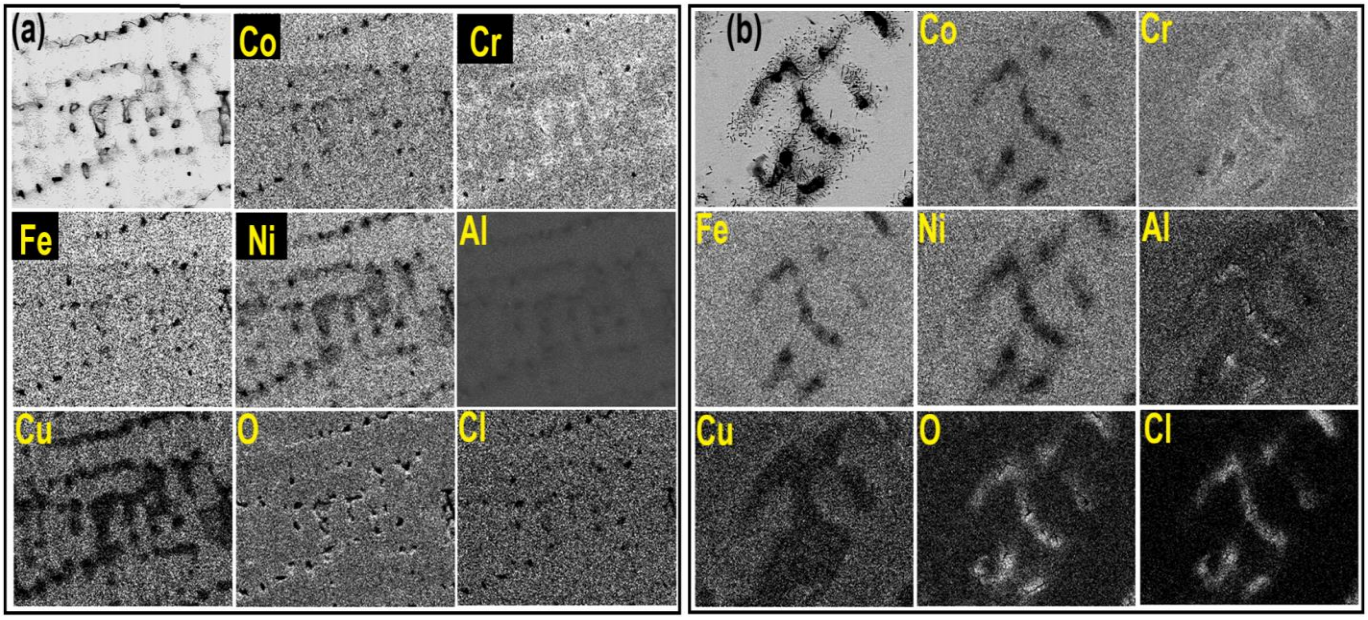

Figure 22. EDS maps of the $CoCrFeNiAl_{0.5}Cu_{0.5}$ surface after the potentiodynamic polarization in the (a) S2 and (b) S3 solutions.

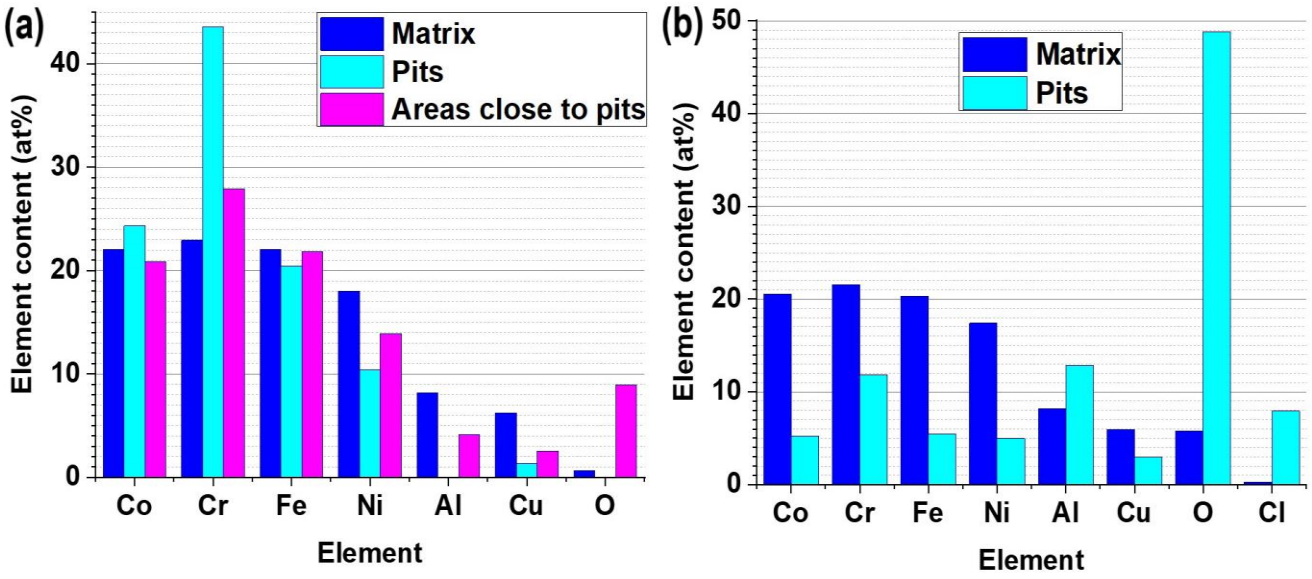

Figure 23. Elemental analysis of the $CoCrFeNiAl_{0.5}Cu_{0.5}$ surface after the potentiodynamic polarization in the (a) S2 and (b) S3 solutions.

In the case of the S2 solution, the presence of corrosion products with an oxygen content of up to 1 at.% at the locations of the matrix and up to 9 at.% at the locations proximate to the pits was revealed. In the case of the S3 solution, the presence of corrosion products with an oxygen content of up to 6 at.% at the locations of the matrix and up to 49 at.% inside the pits was detected. A halo of corrosion products was observed around the local defects. Among all the elements, aluminum and copper dissolved most intensively. Similar to the case of free corrosion, it can be assumed that the pitting initiated at the sites of the Cu-based precipitates.

4. Conclusions

In the acidic NaCl solution, the molybdenum-containing $CoCrFeNiMo_{0.4}$ HEA and SS 316L exhibited higher corrosion rates compared to the SS 304 due to the uneven distribution of Cr and Mo in the HEA's microstructure and due to the lower Cr content in the SS 316L. For these reasons, in the case of the molybdenum-containing alloys, the acceleration of the selective dissolution might occur at the initial stage of corrosion, before the stabilization of the stationary passive state. In the acidic NaCl solution containing 10 mM H_2O_2 and in the 0.4 M $FeCl_3$ solution, the SSs 304 and 316L were slightly susceptible to pitting and considerably susceptible to intergranular corrosion, while only the small local defects were found on the $CoCrFeNiMo_{0.4}$ surface in the matrix areas proximate to the σ-phase and depleted in molybdenum. The general corrosion rate of the $CoCrFeNiMo_{0.4}$ HEA in the 0.4 M $FeCl_3$ solution was significantly lower than those of SSs. According to the $CoCrFeNiMo_{0.4}$ anodic polarization curve, the alloy's weight losses during the long-term corrosion tests could be also associated with the initiation of metastable pitting. The distribution of chromium and molybdenum in the microstructure of $CoCrFeNiMo_{0.4}$ along with the small σ-phase content provided effective passivation of the surface. As a result, the alloy exhibited high corrosion resistance regardless of the oxidizer and chloride concentrations. When the concentration of Mo in the alloy was higher (CoCrFeNiMo), the intense selective dissolution of the FCC matrix occurred in the presence of the strong oxidizers. The $CoCrFeNiAl_{0.5}Cu_{0.5}$ HEA was not capable of passivation in any test solution, and the presence of an oxidizer intensified its active dissolution initiated at the locations of the Cu-based precipitates. The analysis of polarization curves gave the results qualitatively similar to those of the gravimetric tests in terms of comparative assessment of the alloys' corrosion resistance. However, quantitative discrepancies might arise between the corrosion current density and corrosion rate due to the onset of a steady state during the long-term tests and to the determination of the average corrosion rate rather than the instantaneous one. This phenomenon should be carefully considered when justifying the alloys' potential applications.

CRediT Author Statement

V.A. Vorkel: formal analysis, investigation, methodology, validation, writing – original draft, writing – review & editing, visualization.

R.I. Bogdanov: conceptualization, formal analysis, methodology, validation, writing – original draft, writing – review & editing.
N.A. Pukhareva: investigation, validation.
V.E. Ignatenko: methodology, investigation, validation, writing – review & editing.
A.A. Rybkina: investigation, methodology, validation, writing – review & editing.
A.V. Voennov: investigation, validation.
A.I. Marshakov: methodology, conceptualization, validation, writing – review & editing, supervision, project administration.

Declaration of Competing Interest

The authors declare that they have no known competing financial interests or personal relationships that could have appeared to influence the work reported in this paper.

Acknowledgments

This research did not receive any specific grant from funding agencies in the public, commercial, or not-for-profit sectors.

References

1. Q. Fan, B. Li and Y. Zhang, Influence of Al and Cu elements on the microstructure and properties of (FeCrNiCo)Al_xCu_y high-entropy alloys, *J. Alloys Compd*., **614**, 2014, 203–210. doi: 10.1016/j.jallcom.2014.06.090
2. Z. Niu, Y. Wang, C. Geng, J. Xu and Y. Wan, Microstructural evolution, mechanical and corrosion behaviors of as-annealed $CoCrFeNiMo_x$ (x = 0, 0.2, 0.5, 0.8, 1) high entropy alloys, *J. Alloys Compd*., 2020, **820**, 153273. doi: 10.1016/j.jallcom.2019.153273
3. Q. Hu, C. Ye, S. Zhang, X. Wang, Z. Du and H. Wang, Mo content-depended competition between Cr_2O_3 enrichment and selective dissolution of $CoCrFeNiMo_x$ high entropy alloys, *npj Mater. Degrad*., 2022, **6**, no. 1, 97. doi: 10.1038/s41529-022-00313-6
4. C. Dai, T. Zhao, C. Du, Y. Li and D. Zhang, Effect of molybdenum content on the microstructure and corrosion behavior of $FeCoCrNiMo_x$ high-entropy alloys, *J. Mater. Sci. Technol*., 2020, **46**, 64–73. doi: 10.1016/j.jmst.2019.10.020
5. X. Wang, D. Mercier, Y. Danard, T. Rieger, L. Perrière, M. Laurent-Brocq, I. Guillot, V. Maurice and P. Marcus, Enhanced passivity of Cr-Fe-Co-Ni-Mo multi-component single-phase face-centred cubic alloys: design, production and corrosion behaviour, *Corros. Sci*., 2022, **200**, 110233. doi: 10.1016/j.corsci.2022.110233
6. X. Wang, D. Mercier, S. Zanna, A. Seyeux, L. Perrière, M. Laurent-Brocq, I. Guillot, V. Maurice and P. Marcus, Origin of enhanced passivity of Cr–Fe–Co–Ni–Mo multi-principal element alloy surfaces, *npj Mater. Degrad*., 2023, **7**, no. 1, 13. doi: 10.1038/s41529-023-00330-z

7. Z. Wang, Z. Liu, J. Jin, D. Tang and L. Zhang, Selective corrosion mechanism of CoCrFeMoNi high-entropy alloy in the transpassive region based on the passive film characterization by ToF-SIMS, *Corros. Sci*., 2023, **218**, 111206. doi: 10.1016/j.corsci.2023.111206
8. C. Nascimento, U. Donatus, C. Ríos, M. De Oliveira and R. Antunes, A review on corrosion of high entropy alloys: exploring the interplay between corrosion properties, alloy composition, passive film stability and materials selection, *Mater. Res*., 2022, **25**. doi: 10.1590/1980-5373-mr-2021-0442
9. J. Liang, Q. Wang, Z. Cao, J. Guo, Z. Sun and Y. Hai, Corrosion resistance and mechanism of high-entropy alloys: a review, *Mater. Corros*., 2024, **75**, no. 4, 424–432. doi: 10.1002/maco.202313975
10. Y. Fu, C. Dai, H. Luo, D. Li, C. Du and Y. Li, The corrosion behavior and film properties of Al-containing high-entropy alloys in acidic solutions, *Appl. Surf. Sci*., 2021, **560**, 149854. doi: 10.1016/j.apsusc.2021.149854
11. W. Liang and W. Qin, Corrosion mechanism of eutectic high-entropy alloy induced by micro-galvanic corrosion in sulfuric acid solution, *Corros. Sci*., 2022, **206**, 110525. doi: 10.1016/j.corsci.2022.110525
12. L. Song, W. Hu, X. Zhang, B. Liao, W. Shan, L. Kang and X. Guo, Corrosion behavior of the $AlCoCrFeNi_{2.1}$ eutectic high-entropy alloy in chloride-containing sulfuric acid solutions at different temperatures, *Materials*, 2022, **15**, no. 14, 4822. doi: 10.3390/ma15144822
13. B. Li, K. Peng, A. Hu, L. Zhou, J. Zhu and D. Li, Structure and properties of $FeCoNiCrCu_{0.5}Al_x$ high-entropy alloy, *Trans. Nonferrous Met. Soc. China*, 2013, **23**, no. 3, 735–741. doi: 10.1016/s1003-6326(13)62523-6
14. N. Li, H. Zhang, L. Wu, Z. Li, H. Fu, D. Ni, P. Xue, F. Liu, B. Xiao and Z. Ma, Simultaneously increasing mechanical and corrosion properties in CoCrFeNiCu high entropy alloy via friction stir processing with an improved hemispherical convex tool, *Mater. Charact*., 2023, **203**, 113143. doi: 10.1016/j.matchar.2023.113143
15. X. Chen, H. Qian, Y. Lou, B. Yang, T. Cui and D. Zhang, Effects of Cu-content and passivation treatment on the corrosion resistance of $Al_{0.3}Cu_xCoCrFeNi$ high-entropy alloys, *J. Alloys Compd*., 2022, **920**, 165956. doi: 10.1016/j.jallcom.2022.165956
16. C. Tsai, M. Tsai, J. Yeh and C. Yang, Effect of temperature on mechanical properties of $Al_{0.5}CoCrCuFeNi$ wrought alloy, *J. Alloys Compd*., 2010, **490**, no. 1–2, 160–165. doi: 10.1016/j.jallcom.2009.10.088
17. K. Zhang, Z. Fu, J. Zhang, J. Shi, W. Wang, H. Wang, Y. Wang and Q. Zhang, Annealing on the structure and properties evolution of the CoCrFeNiCuAl high-entropy alloy, *J. Alloys Compd*., 2010, **502**, no. 2, 295–299. doi: 10.1016/j.jallcom.2009.11.104
18. R. Bogdanov, V. Vorkel, V. Ignatenko, M. Gavrushina, A. Voennov, S. Teplyakova, D. Bachurina, O. Sevrukov and A. Marshakov, Corrosion and electrochemical behavior of CoCrFeNiMo high-entropy alloy in acidic oxidizing and neutral chloride solutions, *Mater. Chem. Phys*., 2023, **295**, 127123. doi: 10.1016/j.matchemphys.2022.127123

19. ASTM Standard A240/240M – 20a, ASTM, 2016. PA
20. ASTM Standard G31-72, ASTM, 2004. PA
21. S. Gorsse, M. Nguyen, O. Senkov and D. Miracle, Database on the mechanical properties of high entropy alloys and complex concentrated alloys, *Data Brief*, 2018, **21**, 2664–2678. doi: 10.1016/j.dib.2018.11.111
22. ASTM Standard G1-03, ASTM, 2008. PA
23. G. George, H. Shaikh, in *Corrosion of austenitic stainless steels*, Eds.: H. Khatak and B. Raj, Woodhead Publishing Limited, Sawston, Cambridge, 2002, p. 17. Link
24. T. Shun, L. Chang and M. Shiu, Microstructures and mechanical properties of multiprincipal component CoCrFeNiTi$_x$ alloys, *Mater. Sci. Eng.*, 2012, **556**, 170–174. doi: 10.1016/j.msea.2012.06.075
25. H. Jin, J. Zhang, P. Li, Y. Zhang, W. Zhang, J. Qin, L. Wang, H. Long, W. Li, R. Shao, E. Ma, Z. Zhang and X. Han, Atomistic mechanism of phase transformation between topologically close-packed complex intermetallics, *Nat. Commun.*, 2022, **13**, no. 1, 2487. doi: 10.1038/s41467-022-30040-0
26. X. Chen, T. Cui, S. He, W. Chang, Y. Shi and Y. Lou, Effects of ultrasonic shot peening on the corrosion resistance and antibacterial properties of $Al_{0.3}Cu_{0.5}$CoCrFeNi high-entropy alloys, *Coatings*, 2023, **13**, no. 2, 246. doi: 10.3390/coatings13020246
27. K. Sugimoto and Y. Sawada, The role of molybdenum additions to austenitic stainless steels in the inhibition of pitting in acid chloride solutions, *Corros. Sci.*, 1977, **17**, no. 5, 425–445. doi: 10.1016/0010-938x(77)90032-4
28. J. Wanklyn, The role of molybdenum in the crevice corrosion of stainless steels, *Corros. Sci.*, 1981, **21**, no. 3, 211–225. doi: 10.1016/0010-938x(81)90031-7
29. C. Nascimento, U. Donatus, C. Ríos and R. Antunes, Passive film composition and stability of CoCrFeNi and CoCrFeNiAl high entropy alloys in chloride solution, *Mater. Chem. Phys.*, 2021, **267**, 124582. doi: 10.1016/j.matchemphys.2021.124582
30. R. Newman, The dissolution and passivation kinetics of stainless alloys containing molybdenum – I. Coulometric studies of Fe-Cr and Fe-Cr-Mo alloys, *Corros. Sci.*, 1985, **25**, no. 5, 331–339. doi: 10.1016/0010-938x(85)90111-8
31. R. Newman, The dissolution and passivation kinetics of stainless alloys containing molybdenum – II. Dissolution kinetics in artificial pits, *Corros. Sci.*, 1985, **25**, no. 5, 341–350. doi: 10.1016/0010-938x(85)90112-x
32. V. Maurice, H. Peng, L. Klein, A. Seyeux, S. Zanna and P. Marcus, Effects of molybdenum on the composition and nanoscale morphology of passivated austenitic stainless steel surfaces, *Faraday Discuss.*, **180**, 2015, 151–170. doi: 10.1039/c4fd00231h
33. Z. Wang, E. Paschalidou, A. Seyeux, S. Zanna, V. Maurice and P. Marcus, Mechanisms of Cr and Mo enrichments in the passive oxide film on 316L austenitic stainless steel, *Front. Mater.*, 2019, **6**, 232. doi: 10.3389/fmats.2019.00232

34. B. Lynch, Z. Wang, L. Ma, E. Paschalidou, F. Wiame, V. Maurice and P. Marcus, Passivation-Induced Cr and Mo enrichments of 316L stainless steel surfaces and effects of controlled pre-oxidation, *J. Electrochem. Soc*., 2020, **167**, no. 14, 141509. doi: 10.1149/1945-7111/abc727
35. P. Marcus and J. Grimal, The anodic dissolution and passivation of NiCrFe alloys studied by ESCA, *Corros. Sci*., 1992, **33**, no. 5, 805–814. doi: 10.1016/0010-938x(92)90113-h
36. X. Zhang, D. Zagidulin and D. Shoesmith, Characterization of film properties on the Ni-Cr-Mo alloy C-2000, *Electrochim. Acta*, 2013, **89**, 814–822. doi: 10.1016/j.electacta.2012.11.029
37. Z. Wang, C. Carrière, A. Seyeux, S. Zanna, D. Mercier and P. Marcus, XPS and ToF-SIMS investigation of native oxides and passive films formed on nickel alloys containing chromium and molybdenum, *J. Electrochem. Soc*., 2021, **168**, no. 4, 041503. doi: 10.1149/1945-7111/abf308
38. V. Maurice and P. Marcus, Molybdenum effects on the stability of passive films unraveled at the nanometer and atomic scales, *npj Mater. Degrad*., 2024, **8**, no. 1, 3. doi: 10.1038/s41529-023-00418-6
39. X. Wang, D. Mercier, S. Zanna, A. Seyeux, L. Perrière, M. Laurent-Brocq, I. Guillot, V. Maurice and P. Marcus, Effects of chloride ions on passive oxide films formed on Cr-Fe-Co-Ni(-Mo) multi-principal element alloy surfaces, *J. Electrochem. Soc*., 2023, **170**, no. 4, 041506. doi: 10.1149/1945-7111/accb10
40. X. Huang, D. Costa, B. Diawara, V. Maurice and P. Marcus, Atomistic insights on enhanced passivity: DFT study of substitutional Mo on Cr_2O_3 and Fe_2O_3 surfaces, *Corros. Sci*., 2023, **224**, 111543. doi: 10.1016/j.corsci.2023.111543
41. ASTM Standard G102-89, ASTM, 2015.
42. M. Pourbaix, *Atlas of Electrochemical Equilibrium in Aqueous Solutions*, 2nd Edn., National Association of Corrosion Engineers, Houston, Texas, 1974, 644 pp.
43. R. Jiang, Y. Wang, X. Wen, C. Chen and J. Zhao, Effect of time on the characteristics of passive film formed on stainless steel, *Appl. Surf. Sci*., **412**, 2017, 214–222. doi: 10.1016/j.apsusc.2017.03.155
44. C. Olsson and D. Landolt, Passive films on stainless steels – chemistry, structure and growth, *Electrochim. Acta*, 2003, **48**, no. 9, 1093–1104. doi: 10.1016/s0013-4686(02)00841-1
45. C. Olsson, S. Malmgren, M. Gorgoi and K. Edström, Quantifying the metal nickel enrichment on stainless steel, *Electrochem. Solid-State Lett*., 2011, **14**, no. 1, C1. doi: 10.1149/1.3509122

♦ ♦ ♦